Dynamics of cylindrically converging precursor plasma flow in wire-array *Z*-pinch experiments

S. C. Bott,[1] S. V. Lebedev,[1] D. J. Ampleford,[2] S. N. Bland,[1] J. P. Chittenden,[1] A. Ciardi,[1] M. G. Haines,[1] C. Jennings,[2] M. Sherlock,[1] G. Hall,[1] J. Rapley,[1] F. N. Beg,[3] and J. Palmer[4]

[1]*The Blackett Laboratory, Imperial College, London SW7 2BW, United Kingdom*

[2]*Sandia National Laboratory, Albuquerque, NM USA*

[3]*Department of Mechanical and Aerospace Engineering, University of California San Diego, California, USA*

[4]*AWE Plc., Aldermaston, RG7 4PR, United Kingdom*

(Received 6 April 2006; revised manuscript received 24 July 2006; published 12 October 2006)

This paper summarizes the present understanding of the processes leading to precursor column formation in cylindrical wire arrays on the 1 MA MAGPIE generator at Imperial College London. Direct experimental measurements of the diameter variation during the collapse and formation phase of the precursor column are presented, along with soft x-ray emission, and quantitative radiography. In addition, data from twisted cylindrical arrays are presented which give additional information on the behavior of coronal plasma generated in wire array *z* pinches. Three stages in precursor column formation are identifiable from the data: broad initial density profile, rapid contraction to small diameter, and slow expansion after formation. The correlation of emission to column diameter variation indicates the contraction phase is a nonlinear collapse resulting from the increasing on-axis density and radiative cooling rate. The variation in the minimum diameter is measured for several array materials, and data show good agreement with a pressure balance model. Comparison of column expansion rates to analytical models allows an estimate of column temperature variation, and estimates of the current in the column are also made. Formation data are in good agreement with both fluid and kinetic modeling, but highlight the need to include collisionless flow in the early time behavior.

DOI: 10.1103/PhysRevE.74.046403 PACS number(s): 52.20.Hv, 52.59.Qy, 52.70.La

I. INTRODUCTION

A wire array *z*-pinch experiment displays several distinct stages throughout its duration, from wire initiation to implosion and x-ray generation. On longer current drive (>100 ns) machines the processes occurring prior to the implosion of the main array mass comprise a significant proportion of the drive time, which presents an opportunity to study these in detail. One of the most interesting phenomena to develop during this period is a remarkably uniform and stable precursor plasma column on the axis of the array. Since its first identification [1], precursor column structures have been observed in a large number of experiments and within a wide range of array parameters [1–3]. The arrival of this mass fraction on the array axis, preimplosion, is due to the formation of a heterogeneous plasma structure from each wire caused by the passing of the drive current: relatively cold wire cores surrounded by a low-density hot coronal plasma [4–7]. The radial $\mathbf{J}\times\mathbf{B}$ force accelerates the coronal plasma towards the axis, while the cold wire cores are continuously ablated. It is the stagnation of this flow at the axis which forms the observed precursor column.

This uniform and stable plasma object by itself deserves some attention due to an interesting combination of plasma physics processes occurring during its formation. These include a transition from collisionless to collisional regimes of interaction of the plasma flow, the effect of radiation cooling on the dynamics of the plasma, and the development of ionization balance. In wire array *z* pinches, the converging plasma flow is often sustained for a long time (>100 ns) and in the precursor column these processes can develop in a quasistationary situation. The high degree of the azimuthal symmetry of the plasma flow in this system makes it an almost ideal test bed for one-dimensional (1D) radiation hydrodynamic codes, and indeed is closely analogous to an existing problem in hydrodynamics: Noh's problem [8]. The formed column is an interesting candidate for high energy density physics (HEDP) experiments, and one can also note a close analogy between the precursor formation in wire array *Z* pinches and stagnation of plasma on axis of symmetry in other systems with converging plasma flows, e.g., of the plasma ablated from the walls of ICF hohlraums [9].

The effect of the precursor plasma flow on the implosion dynamics of wire array *z* pinches and on parameters of the x-ray pulses generated by the implosion is actively debated at present. Among reasons for this interest is the unexpected remarkable performance of large diameter wire arrays, which have relatively large interwire separations (>3 mm) [10]. The core-corona plasma structure and the resulting inward flow of coronal plasma is apparently important even for the arrays with very small interwire separations (~0.21 mm), as follows from experiments [11] on the *Z* facility at SNL, in which a very early arrival of the precursor plasma on the array axis was detected. For these arrays it is difficult to envision formation of a plasma shell this early in the current pulse, and hence the discrete nature of the wires should play an important role in their operation. The prefilling of the interior of an array with the plasma should be taken into account not only for understanding of x-ray pulse generation, where the accretion of mass during implosion may reduce instabilities at the accelerating plasma front, but also in the design of different wire array *z*-pinch loads. This could be especially important for the concepts of dynamic [12] and static wall [13] hohlraums, where the precursor flow can significantly change conditions of the foam targets installed on the array axis [14]. To this end, accumulation of experimen-

tal information on formation and behavior of the precursor plasma in wire array *Z* pinches is required. Experiments with relatively low currents and long rise times can help to highlight important processes, and hence evolve a better understanding of the corresponding physical processes through comparison with computer and analytical models, and should be useful for establishing scaling laws.

In this paper we present an experimental study of the dynamics of the precursor plasma formation in wire array *Z* pinches at the 1 MA current level. The content of the remainder of the paper is as follows. In Sec. II the experimental setup and diagnostics are described. Section III describes the behavior of the precursor plasma and formation of the compact precursor column in cylindrical wire arrays. Data is presented on parameters of the coronal plasma flow in aluminum and tungsten wire arrays, as are discussions on how the difference in the collisionality of the coronal plasma flow for the two materials affects the dynamics of the plasma accumulating on the array axis. Data demonstrating formation times, column diameters, stability time scales, and radiation profiles for several different materials are presented and discussed. In addition, an analytical approach is applied to estimate the current in the precursor, based on the analysis of stability of the precursor column. In Sec. IV data are discussed with reference to current MHD modeling [15] and to a recently published kinetic description of the precursor formation process [16], which provide some insight into the column formation mechanism. Section V describes experiments with twisted wire arrays, which provide some additional information on the behavior of the coronal plasma generated in wire array *z* pinches. Applications of the precursor column are suggested in Sec. VI, and conclusions are presented in Sec. VII.

II. EXPERIMENTAL SETUP AND DIAGNOSTICS

Experiments were carried out on the MAGPIE generator [17] with a peak current of 1 MA and a rise time of 240 ns (10% to 90% rise time is 150 ns), which is closely reconstructed by a $\sin^2$ wave form. Wire arrays 16 mm in diameter and 23 mm long were used in all of the experiments, with four current-return posts situated on a diameter of 15.5 cm. The load area design allows both end-on (along the axis of symmetry) and side-on (radially) diagnosis of the entire array. Experiments were performed with arrays of 8, 16, 32, and 64 Al or W wires of different diameters (10, 15, 50 μm Al, 4, 5, and 7.5, 13 μm W), and in some cases with Ni, Cu, Ti, and Mo wires. Over-massed arrays (50 μm, Al, and 13 μm W) do not implode on the time scale of the experiment, and are used to study the precursor on long time scales. Where imploding loads were used, implosion times for arrays with different number of wires were between 180 and 320 ns, as determined from the optical streak photographs and the onset of the x-ray pulse from the pinch.

In addition to standard cylindrical arrays, twisted arrays are also investigated. For these, the top electrode holding the wires was rotated by $\pi/4$, $3\pi/4$, or $\pi/2$ relative to the bottom electrode. Small angles of rotation do not disturb the array behavior, and can be used to measure the azimuthally averaged radial distribution of the coronal plasma inside the array. For larger angles of rotation, the magnitude of the axial magnetic field generated inside the twisted wire array was large enough to affect the dynamics of the inward flow of the coronal plasma and the formation of the precursor column on the array axis.

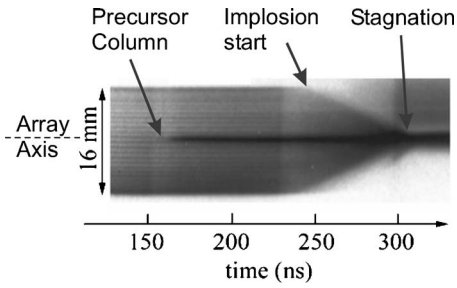

FIG. 1. Radial optical streak photograph showing relative timings of precursor column formation, start of main array implosion, and stagnation.

Diagnostics used in the experiments included laser probing, optical and soft x-ray imaging, a range of filtered x-ray diodes, time and space resolved XUV spectroscopy, and x-ray radiography. Optical probing was performed using a frequency doubled Nd-YAG laser (532 nm) with stimulated Brillioun scattering (SBS) pulse compression (imaging pulse duration ~0.4 ns), and images were recorded on CCD cameras. The laser beam was split to provide simultaneous end-on and side-on measurement, as well as multiple frame times. End-on laser probing provides information about the azimuthal structure and radial distribution of the coronal plasma, and was achieved by installing a mirror into the base of the cathode. The side-on optical diagnostics include laser probing with interferometer, shadow, and Schlieren channels, and a streak camera with its slit oriented along the array radius. The timing of the laser pulse was registered on the optical streak camera, which provided synchronization of optical streaks with other diagnostics. X-ray diagnostics include three gated x-ray cameras (2 ns gate, 9 ns, or 30 ns interframe time) [18], XRD diodes with an aluminum photocathode and photoconducting detectors (PCD) [19] with various filters. The gated x-ray cameras had a spatial resolution typically of 100–200 μm, and for measurements during the run-in phase of implosion were filtered with 1.5–5 μm polycarbonate (transmission window between 150–290 eV). XUV spectroscopy in the range 50–400 Å was performed using a grating (grazing incidence) spectrometer and temporal resolution was achieved by imaging the spectra onto a gated MCP camera with an exposure time of ~10 ns. The use of an additional slit, which formed an image on the input slit of the spectrometer, provided spatial resolution of ~0.5 mm in the radial direction.

III. PRECURSOR COLUMN

A. Precursor column formation

The precursor column is a compact, well defined, strongly emitting object observed to form on the axis of a cylindrical wire array prior to the main implosion phase. Figure 1 shows

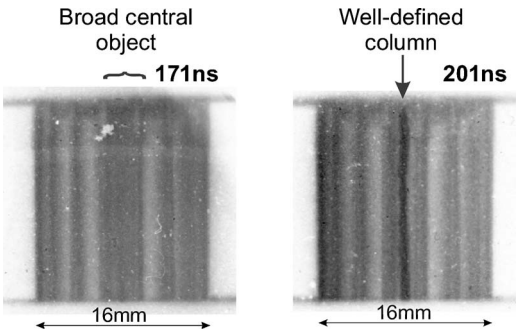

FIG. 2. Side on XUV emission image of a 16 wire tungsten array showing formation of the compact precursor column.

a radial optical streak photograph of a 16 mm diameter aluminum array comprising 64 aluminum wires with a 10 μm diameter. The formation of the precursor column on the array axis occurs at ~160 ns, the start of the implosion of the array at 250 ns and the stagnation of the array on the axis at 300 ns.

The formation of the column is rapid, and observed on all diagnostics at similar times. Figure 2 shows two side-on XUV emission images for a tungsten array taken before and after formation of the compact precursor column from an initially broad emission region. This initial distribution is a result of the interaction of the plasma streams from the individual wires as they converge onto the array axis. The wire cores are stationary at this time and slowly ablate, generating coronal plasma which is continuously injected into the array. In experiments, measurements of the inwards radial velocity of plasma streams in aluminum arrays gives $\sim 1.5 \times 10^5$ ms^{-1} [20], with wire arrays made of other materials yielding comparable values.

The rocket model [21] defines an "ablation velocity" as a constant relating force and the mass ablation rate of the wire cores, and sets this equal to observed plasma stream flow velocity. Data from multiple experiments gives ablation rates consistent with an approximately constant ablation velocity, and the rocket model is widely used in analytical diagnoses of wire array behavior. Computational and theoretical magnetohydrodynamic (MHD) models suggest that stream flow velocity varies with several parameters, including radial position, but that the value as plasma reaches the axis is similar to the ablation velocity inferred from experiment. Given this, a constant ablation velocity can be taken as a representative of the flow velocity where plasma streams interact close to the array axis and the rocket ablation model will be deemed a good approximation for the present study.

The apparent universality of this ablation velocity suggests that the ion kinetic energies ($E_{ion}=0.5m_{ion}V_{abl}^2$) for different materials vary considerably by virtue of their atomic masses. Using $V_{abl}=1.5\times10^5$ ms^{-1} from above, calculated values are ~3 keV for aluminum and ~21 keV for tungsten. The mean free path (mfp) for ion collisions will determine the extent to which counterpropagating plasma streams interact at the array axis, and this varies as the square of the ion kinetic energy. The characteristic scale length of the experiment is the array radius, which was 8 mm for all arrays. A mean free path significantly shorter than this would indicate

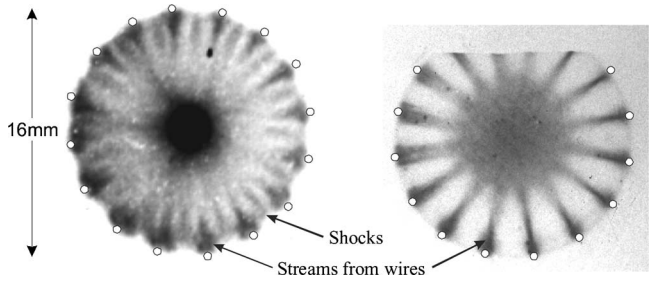

FIG. 3. End-on XUV emission from 16 mm diameter arrays of (left) 16×20 μm Al at 134 ns, and (right) 16×13 μm W at 134 ns. (White circles indicate positions of wires).

that plasma streams would stagnate at the array axis, and a value significantly larger would suggest a low level of interaction, and that counterstreaming behavior would occur.

Plasma streams ablated from the wire cores first reach the axis at ~105 ns, which is a combination of a ~50 ns "dwell time" (during which the core-corona structure is formed), and the time of flight from the array radius to the axis assuming fixed ablation velocity. The rocket model gives ion number densities of $\sim10^{17}$ cm^{-3} for aluminum and 10^{16} cm^{-3} for tungsten. The calculated mean free path values at axis, at this time are then ~0.5 mm for Al ions (assuming $z\sim6$), and ~10 mm for W ions (assuming $z\sim14$). The ablated plasma streams for aluminum should therefore be highly collisional on the scale of the array radius, whereas tungsten streams should display a much lower degree of collisionality. This is in good agreement with formation of shocks where streams from adjacent wires collide, which are seen on laser probing and XUV emission images of Al arrays, and the absence of such features for comparable W arrays (Fig. 3). The plasma streams generate a density profile which is peaked on axis, as a result of both collisions and the convergent geometry, and which continues to rise with increasing stream density during the experiment. During this period, imaging diagnostics observe a broad object on the array axis, with a diameter of several millimeters: i.e., a significant proportion of the initial array diameter (Fig. 4). At some point, the plasma that has converged onto the axis undergoes a rapid contraction in diameter and an associated x-ray output is recorded. The appearance of a well defined narrow column is observed and this is the compact precursor column. The formation time scale of the precursor column is typically <10 ns [22], and diameter of the formed column is characteristic of material, varying inversely with atomic

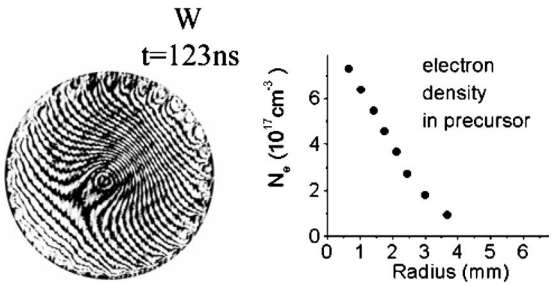

FIG. 4. Laser interferogram of a 16 mm diameter, 16 wire W array at early time and corresponding electron density plot.

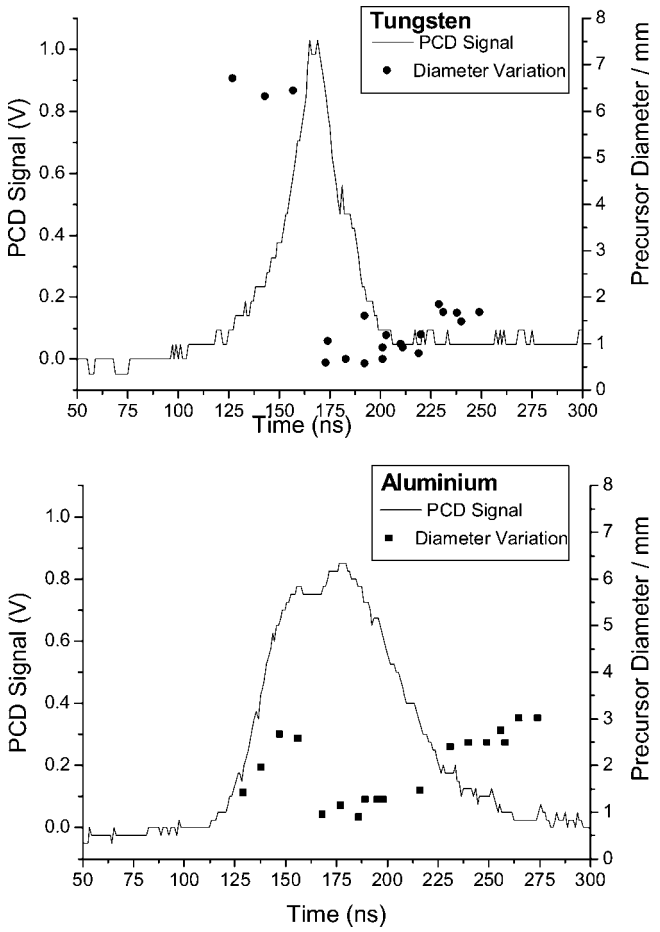

FIG. 5. The variation of precursor diameter with time from XUV imaging, correlated to soft x-ray emission for (top) 16 wire tungsten and (bottom) 32 wire aluminum arrays.

number. The column then remains stationary on the array axis until plasma flow from the wire cores diminishes or the main array mass implodes onto it.

To investigate these processes experimentally, the diameter of the on-axis emission region was monitored for overmassed (nonimploding) aluminum and tungsten cylindrical wire arrays. Gated x-ray cameras were mounted both end-on and side-on, and imaged through 100 μm pinholes that were either unfiltered ($h\nu > 40$ eV) or filtered with 2 μm polycarbonate film ($h\nu \sim 200-280$ eV). PCD traces, both unfiltered and filtered with the same polycarbonate film, were also recorded during the experiments to correlate the array soft x-ray emission with the XUV images. The diagnostics were afforded a full view of the array in each orientation.

The variation of the diameter and typical PCD traces taken over a series of experiments are given in Fig. 5. PCD traces were observed to be repeatable to within ±5 ns, and the features discussed below were reproduced in each experiment. The variation in diameter occurs similarly for both materials, and three distinct stages in the diameter evolution can be identified: (i) broad initial density profile, (ii) rapid contraction to small diameter, (iii) expansion of column following formation. The initial diameters are significantly different for aluminum and tungsten. In Fig. 5, aluminum shows an increasing diameter from ~110 ns, similar to the first arrival of plasma at the array axis, and reaches a maximum of ~3 mm before the rapid contraction phase. Tungsten, however, shows a diameter of ~7 mm from early times, which remains relatively constant until collapse occurs. This is a direct result of the collisionality differences discussed above. Tungsten ions are less confined to the array axis and counterstream for some time, and so a broader emission region is observed. Aluminum ions essentially stagnate at the axis, forming a more confined emission region.

The contraction phase and appearance of the precursor column occurs noticeably earlier in the current drive for aluminum (150–160 ns) than for tungsten (160–175 ns). This process occurs over approximately 10–15 ns for both materials, and this corresponds to collapse rates of the order of the ablation velocity, although present results do not allow an exact measurement. The average collapsed diameters are 1.6 mm for aluminum and 0.6 mm for tungsten. Following formation, both aluminum and tungsten columns are observed to continually increase in diameter for the remainder of the experiment. This expansion is discussed in more detail in Sec. III B.

The x-ray signal from tungsten arrays shows several features. A slow start to the emission begins at ~100 ns and rises increasingly rapidly to a peak at 175 ns. Following the peak, the signal then drops rapidly to a low, but non-zero level some 40 ns later. The FWHM of the signal is ~25 ns. Aluminum shows a similar rise, but has a double peaked structure, with the first peak at 155 ns and the second at 180 ns. The FWHM of this is ~70 ns, and the signal level subsequently drops to zero. It should be noted that the stagnation of an imploding array on MAGPIE produces a signal in this energy band 20–30 times greater than that of the precursor formation signal shown in Fig. 5.

The appearance of the compact precursor column, i.e., when the smallest diameter is observed, occurs at or shortly after the first "formation" x-ray peak (within errors) in both materials for the data discussed above. The formation mechanism can be further examined by correlating the PCD traces to end-on XUV images, both filtered with 2 μm polycarbonate film, taken during column formation. This is shown for a tungsten array in Fig. 6. The first filtered XUV image shows a large diameter (5.7 mm) object during the initial x-ray rise. By the time of the second image, at 186 ns, the x-ray emission is falling and this object has contracted to ~3 mm. Figure 5 indicates that the time of collapse is of the order of 10 ns, as shown above, and so this contraction is unlikely to have started prior to the x-ray peak at 170 ns. This is confirmed by the unfiltered image taken at 168 ns on the same shot, which shows the broad initial density profile is still present at this time, and hence little contraction has occurred by the time of peak x-ray emission. The filtered XUV image at 216 ns shows a very narrow object with a diameter of 0.6 mm, which shows only a low level of emission through the filter. This is the fully formed precursor column.

Given that the formation of the precursor column is observed to form in similar ways for both materials it is likely that the radiation signature represents the same mechanism for aluminum and tungsten, but that the material properties

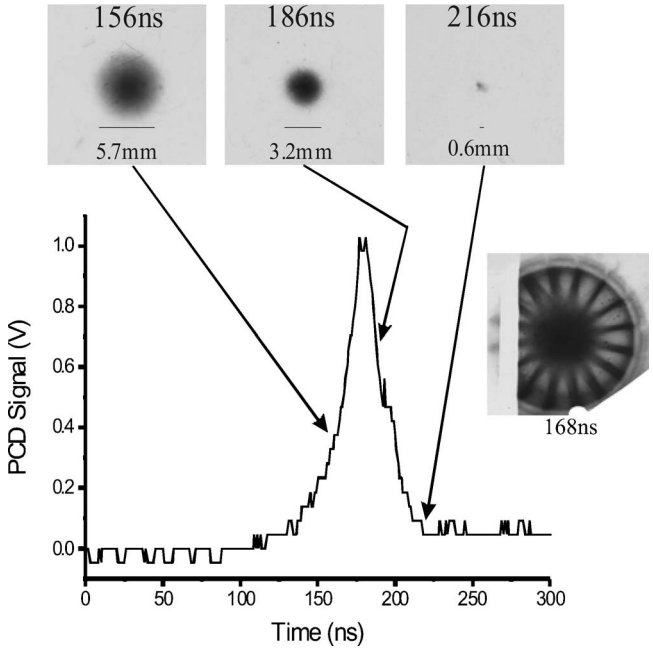

FIG. 6. Filtered end-on XUV images correlated to PCD trace (with the same filter) during precursor column formation for a 16 wire tungsten array, and (single image right) unfiltered end-on XUV image at peak x-ray signal, 168 ns, showing broad density profile.

vary its exact form. With reference to the data presented in Figs. 2–6 it is possible to construct a likely mechanism for the formation process. At early times, the onset of collisionality between highly energetic ions, and subsequent energy transfer to electrons, begins to heat the plasma on axis. If the thermal pressure of the central plasma object is comparable to the kinetic pressure of the ablated plasma streams, it could not be compressed at this time and would remain at some relatively large diameter. As the density of the incoming streams increases with the drive current, the increased kinetic pressure forces density at the axis to slowly rise. The substantial thermal pressure, however, does not allow a reduction in diameter of the central plasma object. The level of radiation emitted from the central plasma will increase as the density rises. Since the radiation loss rate is proportional to the square of the ion density, the measured output would rise increasingly rapidly. Eventually the energy being radiated will exceed the energy thermalized by the incoming plasma streams, and the central plasma object can begin to cool. This effect will be greatest where density is highest, i.e., at the axis in cylindrical geometry. Where cooling has occurred the kinetic pressure can compress the plasma, generating higher density and increasing the radiation loss, and a run-away collapse process is initiated. The density profile would be compressed onto the axis, generating the high density precursor column.

These mechanisms will be dependent on the array material, which may alter the significance or timing of each event. If this physical picture is correct, the total energy radiated by the time collapse begins, i.e., by the peak of filtered x-ray signal in Fig 7, should be comparable to the accumulated stagnated kinetic energy of the plasma streams up until this time. Quantification of the radiated energy loss can be

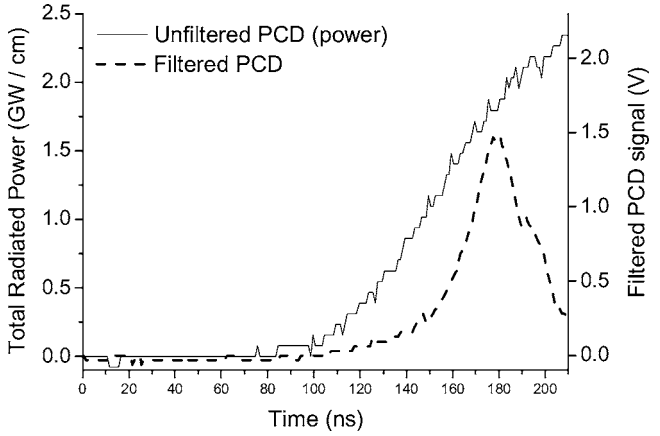

FIG. 7. Total radiated power and filtered PCD signal for a 16 wire tungsten array during precursor column formation.

achieved experimentally by recording the emitted radiation using unfiltered PCDs. These are sensitive to radiation in the range ~4 eV to >3 keV, and so record the total radiated spectrum. Unfortunately this means that the detector saturates rapidly during an experiment, and signals are reliable only for the relatively early stages of the current drive. For tungsten experiments it was possible to obtain unfiltered traces which proved reliable up to the peak of the filtered x-ray signals discussed above (~180 ns). The recorded voltage traces can be converted to power, using the calibrated sensitivity in Ref. [19], and a scaling for the fraction of radiation viewed by the detector gives a total radiated power (assuming isotropic emission). This is shown in Fig. 7. The unfiltered PCD signal begins to rise at ~85 ns and reaches ~4.5 GW/cm at the time of the peak in the filtered PCD signal. For comparison, the stagnation of the main array on MAGPIE produces several hundreds of GW/c of peak radiated power. The integral of the power trace gives the absolute radiated energy, and up to the peak in the filtered x-ray signal this is ~160 J. The calibration of the PCDs is not necessarily exact for the devices used here, and is affected by usage and damage. This figure may therefore be subject to substantial errors, but is sufficient for an order of magnitude estimation. For comparison to this, the rocket ablation model [21] gives a total mass accumulated in the precursor at a given time [see Eqs. (1)–(3) below]. The use of the constant ablation velocity then allows a total "accumulated" kinetic energy in the initial density profile to be calculated. For the kinetic energy of all ions and assuming no energy losses, this value is 185 J.

The energy loss which allows collapse and precursor column formation will comprise contributions from both the radiation loss measured above and ionization processes. To give an indication of the possible contribution from ionization, one can calculate the energy required to ionize all the tungsten on the axis at 180 ns from $z=8$ in the streams to $z=14$. This value is ~15 J, which is small by comparison to the total radiated energy measured. Similar calculations for aluminum suggest the contribution from ionization may form a slightly larger proportion of the total expected, but is again small by comparison to the radiated energy loss. In the formed column the end-on radiation profile becomes hollow,

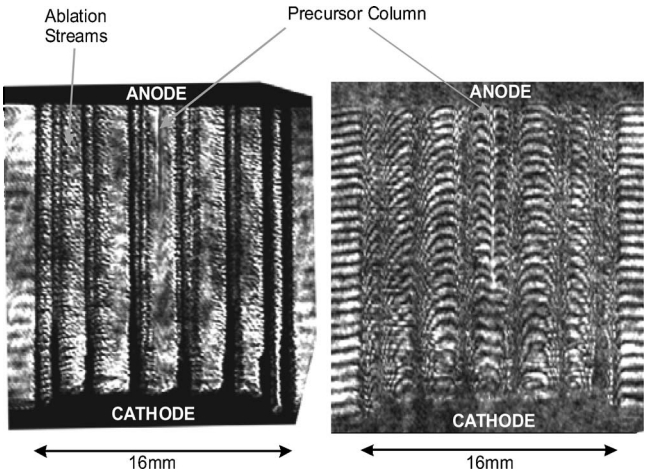

FIG. 8. Laser interferometer and shadow images from the same shot, showing axial nonsimultaneity of a precursor column formation at 160 ns in a 16 wire tungsten array.

as discussed in Sec. III B, and a high temperature (hence higher z) region is only a fraction of the total column volume. In this case, the average charge state may not be significantly different from the stream charge state. It is likely that energy consumed by ionization processes contributes to the column formation, but the present level of accuracy of PCD calculations do not allow a clear determination of this. More accurately calibrated radiation measurements are required to evaluate this contribution.

Once the collapse process has begun, compression then continues until the final precursor diameter is reached. This final diameter is likely to be determined by the balance of the radiative loss and thermal pressure of the plasma with the stream kinetic pressure. These parameters will again vary with material, resulting in a different diameter for different array materials. Further discussions of this are given in Sec. III B below. The first peak in the filtered x-ray signal (Fig. 5) indicates when the formation process is occurring, giving an indication of when the precursor column is forming during an experiment. The second peak is likely to be a result of hydrodynamic bounce, or column compression, both of which would vary with array material. A comparison to modeling results is presented in Sec. IV in order to elucidate a possible mechanism for the form of the x-ray pulse.

Experimental results show that the precursor column is not formed simultaneously at all axial positions. Laser, XUV and visible self-emission imaging all show that the precursor column is initially formed at the anode (Fig. 8), being formed fully to the cathode several nanoseconds later. The delay at different axial positions can be quantified during an experiment by using multiple frame diagnostics to infer a phase velocity of formation in the axial direction. This is of the order $\sim 10^6$ ms^{-1}, assuming linear formation, but experimental values are very limited at present. This delay in formation with axial position is not strongly reflected in the x-ray pulse measured during the formation of the precursor column. Experiments have been carried out using a narrow horizontal slit placed close to the pinch, in front of a PCD with the same filtering and at the same distance as used previously. In this arrangement, the PCD views only a ~ 2 mm horizontal section of the array. If the axial formation delay were significant, a narrowing and timing difference would be expected relative to the x-ray traces presented in Fig. 5, where the full array height is viewed. The resulting traces, however, maintain their relative timings and forms.

It is possible that this difference in formation time is a result of a variation in the wire ablation rate in the z direction. If it is assumed that mass ablation rate varies continuously along the z axis, we can estimate the variation in ablation velocity required to give a zippering of the precursor column of a rate similar to experiments. For a difference of approximately 0.5×10^5 ms^{-1}, the time of flight to the axis for the anode end and cathode end of the array would differ by approximately 20 ns. So, for example, ablation velocity would vary linearly between 1.25×10^5 ms^{-1} and 1.75×10^5 ms^{-1} with the cathode end being the lower of these two velocities. The slightly higher velocity at the anode end would allow formation of the precursor column here first, and the delay of formation at the cathode is then a result of the extended flight time to the axis with a lower velocity. This scenario gives a phase velocity of precursor column formation to be of the order of 10^6 ms^{-1}, similar to experiments. Collisionality issues will also play a role for tungsten arrays, and the lower velocity and greater mass ablated at the cathode end would give a reduced period of collisionless flow here. The phase velocity may therefore be higher than is suggested by the argument above. In aluminum arrays, the ablated plasma streams are collisional on the scale of the array radius from early times, and the delay in formation is directly related to the time of flight to the axis. To give the same column formation phase velocity for both Al and W arrays, the difference in ablation velocities between cathode and anode would need to be greater for W than in Al.

B. Characteristics of the precursor column

This section investigates the behavior of the fully formed precursor column. The rise of the x-ray pulse due to the stagnation of the array on the axis begins when the imploding sheath impacts the precursor [11,23–25], not the bare array axis, and so the precursor properties are important in defining the final stage dynamics of wire arrays.

Following formation, the precursor column continues to radiate in the range 40–200 eV for all the array materials studied. The diameter of the precursor column immediately after formation shows a dependence on array material, as was noted for aluminum and tungsten in the previous section. Several other array materials have been investigated on the MAGPIE generator, and the observed minimum column diameters are plotted in Fig. 9. The average diameter values for each material are shown, with error bars representing the standard deviation. Some materials have been investigated only for a small number of experiments, and so statistical analysis would not be meaningful. Values range from 3 mm for carbon arrays to 0.25 mm for gold arrays. Significantly, the values decrease almost monotonically with increasing atomic number, suggesting that radiative cooling plays an important role. Previous analysis of the variation in the precursor column diameter is presented in Ref. [22], which

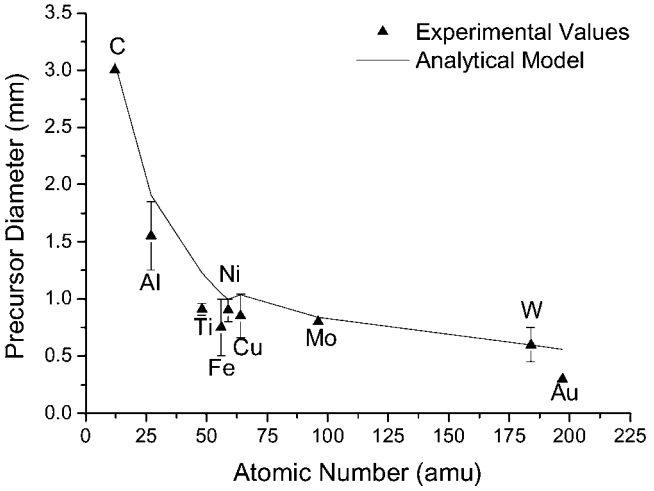

FIG. 9. Variation of precursor diameter immediately after formation with atomic number; Data (▲) are shown with error bars (absence indicates too little data for statistical analysis), along with analytical model estimations (solid line).

leads to a description of how the precursor diameter varies with atomic number. The method is derived from the rocket ablation model which evaluates the mass ablated from the wires in an array at time t as

$$\delta m(t) = \frac{\mu_0}{4\pi V_a R_0}\int_0^t I^2(t)dt, \tag{1}$$

where V_a is the ablation velocity, R_0 is the array radius, and I is the drive current which varies with time, t. From this expression, the mass density inside a given precursor radius, r_p, at time t can be described. This is achieved by adjusting the integral limits to account for the time of flight delay from the wires to the required radius, $t-R_0/V_a$, and dividing by the precursor volume

$$\rho_p(t) = \frac{\mu_0}{4\pi^2 r_p^2 V_a R_0}\int_0^{t-R_0/V_a} I^2(t)dt. \tag{2}$$

To recover the precursor column radius, some simplifications of the physical situation must be made. After formation, it is assumed that the column diameter remains at a radius determined by the balance between the kinetic pressure of the incoming plasma streams and the thermal pressure of the column itself. To allow this situation to exist it must also be assumed that all kinetic energy from the streams is radiated away. The kinetic pressure is given by

$$P_{kin} = \frac{V_a}{2\pi r_p}\frac{dm}{dt} \tag{3}$$

and the thermal pressure is given by $(z+1)N_iT$, where the ion density can be replaced by the precursor density in Eq. (2) divided by the ion mass. If these expressions are then evaluated at the boundary of the precursor column, and so $r=r_p$ in both cases, an expression for the equilibrium radius of the column can be found

$$R_{eq} = \frac{\int_0^{t-R_0/V_a} I^2(t)dt}{I^2[t-R_0/V_a]}\frac{2(z+1)T}{V_a m_{ion}}. \tag{4}$$

Previous experiments on MAGPIE applied radially resolved XUV spectroscopy to estimate the plasma temperature for an aluminum precursor column [22]. These experiments inferred an electron temperature of 50–60 eV, and this value can be used as a guide in the above analysis. To evaluate the relative variation in radius for different materials, a ratio of the expressions derived from Eq. (4) for two materials can be taken. For example, for tungsten and aluminum this gives

$$\frac{R_W}{R_{Al}} = \frac{(Z_W+1)T_W A_{Al}}{(Z_{Al}+1)T_{Al}A_W}. \tag{5}$$

For $Z_W=14$, $Z_{Al}=6$, $T_W=T_{Al}=60$ eV, a ratio of 0.31 is calculated. This compares well with the value from experiments of 0.37 (using the minimum radius values of $R_W \sim 0.3$ mm and $R_{Al}\sim 0.8$ mm).

This simple analysis can be extended to include all the array materials investigated on MAGPIE, and this allows comparison to the experimental data. The calculated variation with atomic number is given by the solid line in Fig. 9. The values for charge states used for the comparison (assuming $T\sim 60$ eV in all cases) are $Z_C=4$, $Z_{Al}=6$, $Z_{Ti,Fe,Ni}=7$, $Z_{Cu}=8$, $Z_{Mo}=10$, $Z_{W,Au}=14$, which are consistent with corona equilibrium (CE) ionization values [26]. Note that the model is normalized to tungsten, and so the ratio in Eq. (5) equates to unity for this material. The experimental column diameter observed immediately after formation compares very well to the diameters expected from this analysis, although the diameter is slightly overestimated for most materials. Despite this, the similarity of experimental and model results suggests that the precursor column is in approximate pressure balance immediately after formation. The expansion at later times discussed in the next section moves experimental values towards, not away from, the model values indicating that the column remains in, or close to, the pressure balance assumed in this model.

Following the formation of the precursor column at its "equilibrium" radius, two processes are observed. The column diameter slowly increases, and the center of the column (viewed end-on) begins to show reduced emission. The latter of these is shown in Fig. 10, which comprises a sequence of end-on XUV images for a tungsten array taken during a single experiment. The plot shows line outs of the emission profile through the array diameter at the image times (note that film contrast has been normalized to the emission observed close to the wire position, at 1 mm and 15 mm, for each image). At 133 ns a broad initial emission profile occupies a large portion of the array diameter, as was reported in Fig. 5. At 163 ns, the highly emitting well-defined precursor column is seen to develop from the broad emission profile, and appears partially formed at this time. At 193 ns the column has been fully formed for ~20 ns and the center of the column radiates less than the region of high emission at its

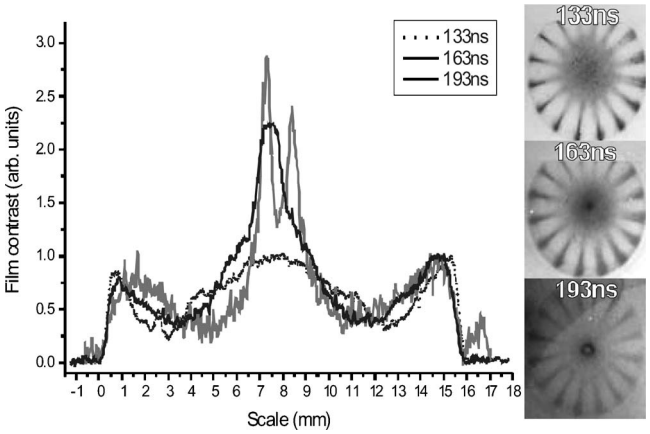

FIG. 10. Development of hollow radiation profile in tungsten precursor column produced in a 16 mm diameter, 16 wire array.

perimeter. This process is observed for both tungsten and aluminum arrays.

The appearance of this hollow radiation profile could be explained in the following way. Once the precursor column has formed, its density is significantly greater than the plasma streams which continue to impact it, and a classic standing shock scenario is realized. The high rate of radiation from the dense column allows rapid cooling of energetic ions following impact at the shock front, i.e., the column radius, and the rate of cooling at a given post-shock velocity yields a cooling length. If the velocity is relatively constant with time, the cooling length will then depend on the density of the column and incident streams, and the ion energy on impact. If the precursor grows in radius and/or density, the cooling length may become shorter than the column radius itself, and so a "hollow" radiation profile may be expected.

The XUV cameras used to image the precursor column in Fig. 10 are sensitive to radiation above ~40 eV. If the center of the column has equilibrated and cooled to below this level, it would be expected that emission at this position in the image would be reduced, as is observed. The region where ions are thermalizing across the shock is typically ~400 μm at times shortly after column formation. At present, there is little data on the variation of this width with time, although it is clear that this will continue to reduce if density continues to rise and may therefore provide an indirect measure of the change in column density with time. It should be noted that this process appears analogous to the radiation cooling signature observed in laser-generated jets [27].

The experimental results presented in Sec. III A show that rather than remaining static at its minimum radius, the precursor column continuously expands for both materials investigated in detail. The variation in diameter after column formation, ~165 ns for Al and ~180 ns for W, are plotted in Fig. 11. The scatter in the data limits analysis to a simple linear fit to give an average expansion rate over the time scale investigated and fitted rates for tungsten and aluminum are 2.5 μm/ns and 10 μm/ns, respectively.

Since the column is expanding with time, the analyses presented above cannot be directly applied for times subsequent to moment of formation. We can, however, apply simi-

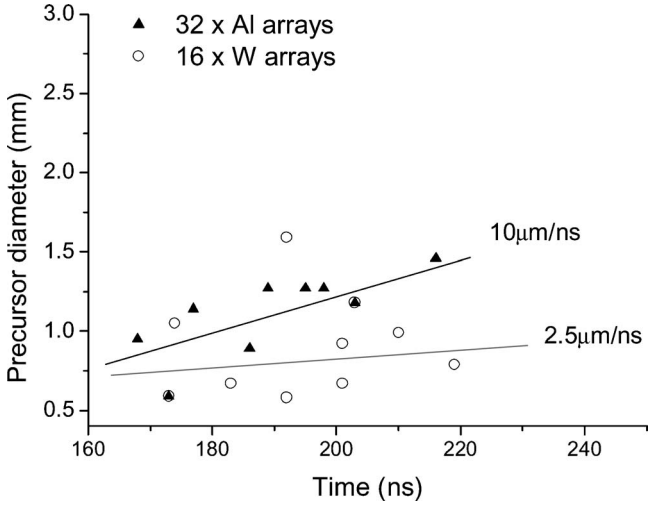

FIG. 11. Observed growth rates for (top) aluminum and (bottom) tungsten precursor columns after formation, with straight line fits.

lar methods with slightly different assumptions. Despite the requirement that the column is static, the above discussions allow a good estimate of the precursor diameter at formation, and suggests thermal and kinetic pressures are balanced. After column formation, plasma streams continue to arrive at the precursor column edge, increasing the mass accumulated in the column. The evolution of the column can therefore occur broadly in two ways: with constant radius and increasing density, or constant density and increasing radius. The former of these is clearly not occurring here and so the assumption of constant density will be investigated for comparison to the observed expansion rates.

For a given precursor column radius an average density can be calculated at the observed time of formation from Eq. (3). If density remains constant from this time on and the column remains in approximate pressure balance, the column will grow in radius as mass continues to arrive. Reference [16] derives the rate of change of the column radius from the rocket ablation model as:

$$\frac{\partial R_p}{\partial t} = \left(\frac{\mu_0}{4\pi^2 m_i n_i V_a R_0}\right)^{1/2} \frac{\partial}{\partial t}\left(\int_0^{t-R_0/V_a} I^2(t)dt\right)^{1/2}. \quad (6)$$

(Note that the equation given in Ref. [16] has been corrected by the original author to the above version.). Due to the lack of a reliable experimental measurement at present, the ion density is taken at column formation from the model described in the reference to be $n_i \sim 3\times 10^{19}$ cm^{-3}. If this value is used, an expected growth rate can be found which varies as the square root of the ion masses for different materials. The use of the model density is not ideal and will clearly influence the calculated growth rate. The additional experimental studies of density suggested below would be valuable here, and would also provide direct experimental evidence on whether constant density is a reasonable assumption.

An alternative approach is to continue the pressure balance scenario resulting in Eq. (2). An expression for the pre-

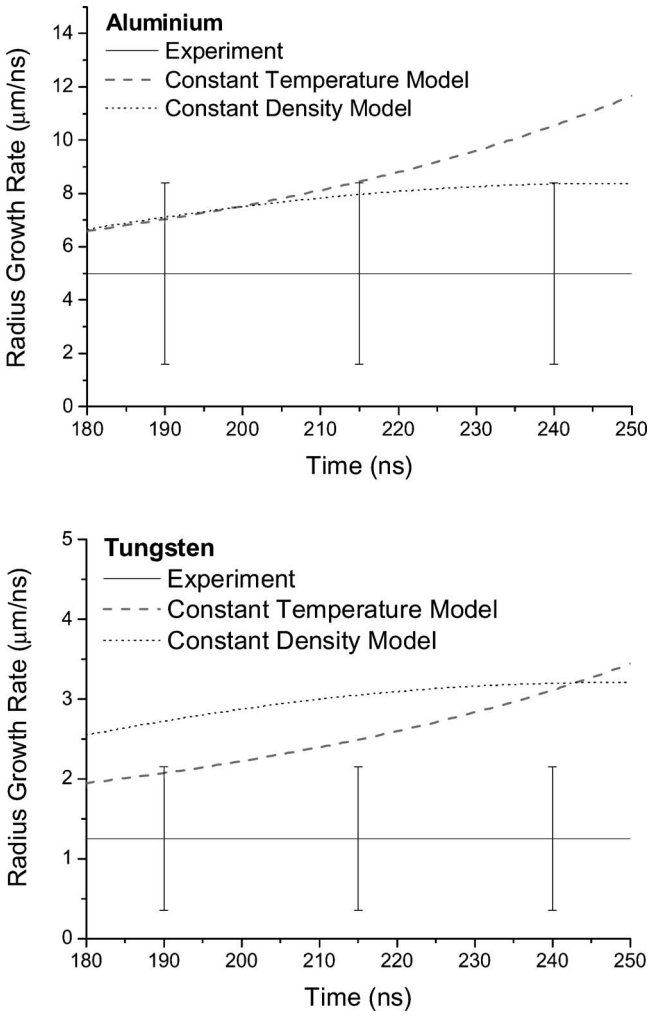

FIG. 12. Experimental values for (top) aluminum and (bottom) tungsten precursor column growth rates compared to simple models assuming constant density and constant temperature. Bars represent error ranges on experimental values.

cursor column radius is given by Eq. (3), and this is independent of the column density, which was problematic in the method above. A temperature must be provided, but around the time of formation this is ~60 eV for aluminum, as discussed previously. If we assume this temperature remains constant, the column radius will change as a function of the mass accumulation described by the first term, and a rate of change can be calculated for aluminum

$$\frac{\partial R_p}{\partial t} = \frac{2(z+1)T}{V_a m_{ion}} \frac{\partial}{\partial t} \left(\frac{\int_0^{t-R_0/V_a} I^2(t)dt}{I^2[t-R_0/V_a]} \right). \quad (7)$$

A rate for tungsten can be evaluated if it is assumed that the tungsten precursor column also remains at ~60 eV. The ionization states used for Eq. (5) are again used here. These two approaches can be compared to the experimentally observed rates to examine which of the two cases is more likely to be occurring in the precursor column expansion phase. This is shown in Fig. 12.

Both models predict that the growth rate for aluminum will be greater than that for tungsten, as a result of the difference in ion mass, and this is consistent with observations. For aluminum, during the period 180–215 ns both models show values which are within the errors of the experimental data. Following this, the constant density model remains at the limit of the errors on the data, while the constant temperature model increasingly deviates from this. For tungsten, the constant density approach consistently overestimates the growth rate. The constant temperature model agrees at early times, 180–200 ns, but again disagrees at late times. The relatively large errors from the experimental measurements do not allow a deduction of the trend in the precursor column growth rate, which could feasibly distinguish between the two simple models presented here. A more detailed study is required to reduce these errors.

The fact that the constant temperature model increasingly deviates from data in both cases suggests that this assumption becomes more inaccurate, and hence that the column may be cooling with time. This is consistent with the x-ray signals and the XUV filtered images presented earlier. If the tungsten precursor temperature is taken as lower than the aluminum precursor, the constant temperature model curve moves into closer agreement with experiment. If tungsten and aluminum column temperatures are indeed comparable, the agreement with experiment for tungsten is lost at an earlier time, perhaps suggesting a greater cooling rate with respect to the aluminum column. It seems likely that any inferred temperature drop with time is associated with some increase in the density of the column, and that both of these factors determine the growth rate following formation. This effect appears more pronounced in tungsten than in aluminum, where density may remain close to constant after formation. Both these simple models vary as the inverse of the ion mass, and so the majority of array materials would be expected to display a precursor column expansion rate between that of aluminum and tungsten.

Since the discussion presented above suggests that the precursor cools with time, an interesting approach is to use the experimentally measured rate of column expansion presented in Fig. 12 to determine this temperature variation. If these values are substituted for dR_p/dt in Eq. (7), and again V_a is 1.5×10^{-5} ms^{-1}, the product $(z+1)T$ can be recovered for both aluminum and tungsten given the correct current wave form, and a charge state. The variation of $(z+1)T$, and the precursor temperature on MAGPIE assuming both coronal equilibrium (CE) and local thermal equilibrium (LTE) ionization models are given in Fig. 13.

Both materials show a decreasing temperature with time, as may be expected from the discussion above. The initial temperatures using LTE ionization are similar to the ~60 eV determined from aluminum experiments, with results from CE ionization slightly higher than this. Both are quantitatively similar despite the use of a simple pressure balance model. The difference of ~20% in temperature between aluminum and tungsten does not appear unreasonable, and other materials would be expected to fall between these two

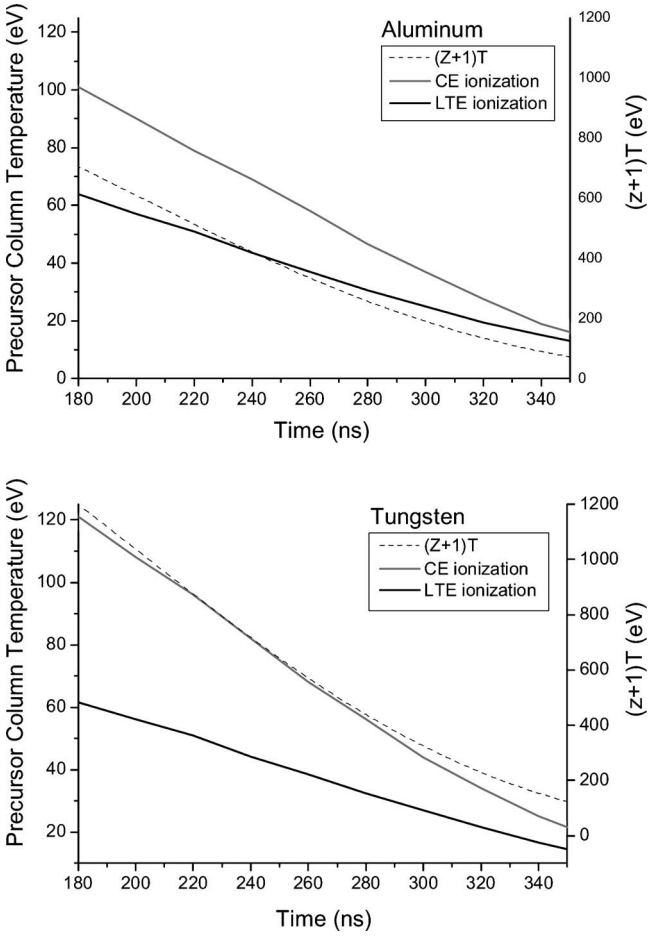

FIG. 13. Variation of the product $(z+1)T$ and precursor column temperature with time using coronal equilibrium (CE) and local thermal equilibrium (LTE) ionization models for (top) aluminum and (bottom) tungsten.

extremes. Between 180 ns and 280 ns after current start an approximately linear temperature decrease occurs, and approximate cooling rates for Al are 0.55 eV/ns (CE) and 0.34 eV/ns (LTE), and for tungsten are 0.65 eV/ns (CE) and 0.29 eV/ns (LTE). As above, additional experiments to more accurately determine the rate of expansion of the column after formation as well as additional XUV spectral data would increase the confidence in this determination of the column temperature variation.

The use of nonimploding arrays with the relatively long rise time and good diagnostic access afforded on MAGPIE allows analysis of the expansion rates of the precursor column without the additional complication of the main array implosion. For imploding loads, the main array mass snow ploughs onto the precursor column and a large fraction of the generated radiation is trapped inside this converging piston. This will increasingly raise the thermal energy of the precursor column, and therefore increase the column expansion rate during the implosion phase. Cuneo *et al.* have investigated this hohlraum effect on the precursor column for tungsten arrays on the *Z* machine [11]. The high opacity of an imploding 300 wire array causes a significant expansion of the precursor column, the start of which is coincident with the onset

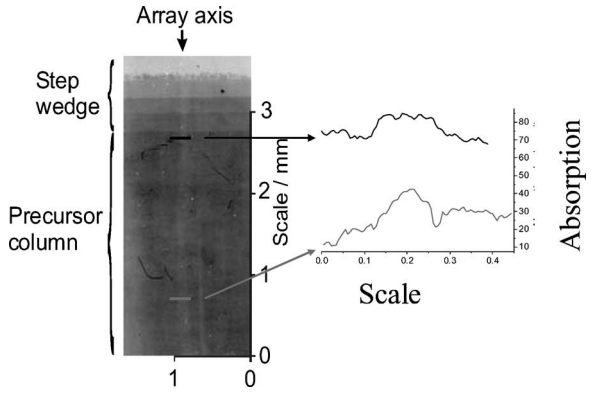

FIG. 14. Radiograph of precursor column for a 16 wire tungsten array with Line outs at indicated positions.

of the main array implosion from its initial diameter. This reference also develops an analytical model relating the precursor expansion rate to the radiated power of the imploding piston, which matches closely with the experimentally observed precursor column diameter change during implosion.

Direct measurements of precursor column density and profile can be achieved using quantitative radiography. An *x* pinch ([28] and references therein), mounted in one of the current return posts, provides high spatial resolution point projection backlighting of the array axis. This image is projected onto a film pack comprising a radiation filter (12.5 μm titanium transmitting 3–5 keV radiation) and a film (Kodak M100) placed immediately behind the filter. Quantitative measurements were taken for a tungsten array, by comparing transmission through the precursor column to that of a step wedge comprising 15 nm, 30 nm, and 45 nm thicknesses of tungsten deposited directly onto the titanium radiation filter. This is presented in Fig. 14. Spatial resolution in this image is better than 5 μm, and exposure time is $\sim$1–2 ns.

The timing of the radiograph is unclear from this experiment, however a statistical analysis of similar *x* pinches on MAGPIE gives an average value of 200±20 ns. Line outs of the image at the indicated positions are also given in Fig. 14, and the absorption profile gives an average areal density of 2×10^{-4} kg/m across the precursor column. The areal density sensitivity limit for the diagnostic is $\sim1\times10^{-4}$ kg m^{-2} (equivalent to 5 nm of tungsten at solid density). The integral of these mass density profiles yields a mass per unit length of 3.6×10^{-7} kg/m at this time, which represents approximately 3% of a typical imploding array (32×5 μm tungsten wires). Analytical calculations from the rocket model [22] suggest the mass fraction in the precursor over this time range is 6–18 %. This discrepancy may be due to several factors. The lack of an accurate time for the radiograph is problematic, and it is possible that the column is still at the early stages of formation. This may account for the observed differences in the radial profile of the column at different axial positions. If the column is indeed fully formed at the time of the radiograph in Fig. 14, some regions may be below the sensitivity limit indicating a radial variation in density in the column. A study of the density profile of the precursor column would increase the current understanding of

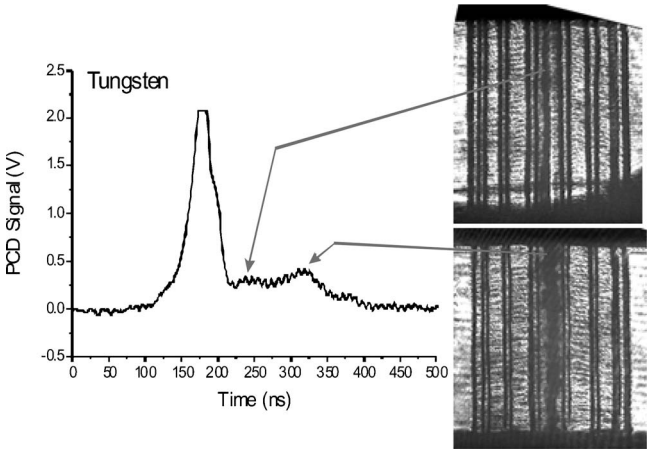

FIG. 15. X-ray signals and laser shadowgraphy showing development of MHD instability structures in tungsten precursor at late time.

wire ablation and precursor column formation, and provide density values to compare to computational codes.

C. Current in the precursor

Previous work [22] noted the remarkable stability of the precursor column over the duration of the experiment. Data from the laser probing and soft x-ray imaging showed that development of the MHD instabilities ($M=0,1$) in the precursor column are not seen for either aluminum or tungsten, and the plasma column remains stable for 100–150 ns. More recent studies show that at very late time W arrays do display some level of instability. The filtered x-ray pulse (as in Fig. 5) for nonimploding tungsten arrays show a "foot pulse" feature, at ~320 ns. Laser shadowgrams taken at the peak of this feature apparently show $M=0,1$ type-structures, as shown in Fig. 15. Similar features are not observed in aluminum precursor columns, either in x-ray signals or imaging diagnostics, at times as late as 300 ns after column formation. This information can be used to obtain an upper estimate of the current which might flow through this plasma, assuming that the growth time of the classical MHD instabilities would be given by these time scales.

Characteristic growth rates of $m=0,1$ instabilities in a Z pinch can be written as [29]

$$\gamma = \left[\frac{c_A}{r_0}\right]\Gamma, \tag{8}$$

where $c_A=\frac{B}{\sqrt{\mu\rho}}$ is the Alfven speed; r_0 is the plasma radius; and Γ is a scaling factor which depends on the instability mode, kr_0 and the distribution of current. Substituting for $B=\mu I/2\pi r_0$ and mass accumulated in the precursor (per unit length) $m_{pr}=\rho\pi r_0^2$ gives

$$\gamma = \left[\frac{c_A}{r_0}\right]\Gamma = \left[\frac{I}{2r}\sqrt{\frac{\mu}{\pi m_{pr}}}\right]\Gamma. \tag{9}$$

The upper estimate of the current which might flow through the aluminum precursor column could be obtained using $1/\gamma > 300$ ns, $r_0=1$ mm, and $m_{pr}<4\times10^{-6}$ kg/m, which is ~50% of the initial mass of a 16×15 μm Al wire array. Taking the wavelength of any instabilities in the precursor to be determined by the coronal streams as 0.5 mm, the minimum value of Γ is ~0.9 (corresponding to a $m=1$ mode with uniform current distribution). Hence, maximum current through the precursor column is less than ~23 KA or $<\sim2.3\%$ of the total current through the array. Here the mass accumulated in the precursor is deliberately overestimated, and the use of smaller mass will give a smaller upper limit of the current. The laser probing measurements presented earlier gave the precursor mass equal to ~2% of the array mass at ~150 ns, while later in time, this mass could be as high as ~10% [22]. Use of the smaller mass of the precursor, corresponding to ~10% of the mass of 16×15 μm Al array, reduces the above estimate of the upper limit of current in the precursor to <1% of the total current. This is in good agreement with direct experimental measurements of the current on-axis during 16 wire experiments, in which a sensitivity limited value of <2% of the drive current was obtained [30].

In tungsten, the development of MHD instability structures are observed at late time, some 130 ns after column formation. If we take the growth time to be 100 ns, $r=0.3$ mm, and use 50% and 10% of the mass of an array, we obtain ~2% and <1% of the drive current respectively. These current estimations are not sufficient to provide containment of the column, which is consistent with the assumptions in the pressure balance condition used in the previous section.

The situation, however, could be different for some other materials, resulting in a higher current fraction. This follows from our preliminary experiments with Ni wire arrays composed of 8 wires [31], in which development of $m=1$ instabilities with characteristic growth time of ~50 ns was observed in the precursor. This indicates that as much as ~30% of the total current could flow through the precursor column in this case. This is consistent with the delay of the implosion observed for Ni wire arrays, and the implosion time measured from optical streak photographs for Ni arrays was ~50 ns or 20% longer than it should be according to zero-dimensional (0D) analysis. In contrast, both W and Al arrays showed implosion times were in good agreement with 0D prediction. Other factors may also influence the current fraction present in the precursor. In 4-wire tungsten arrays on MAGPIE, rapid development of instabilities in the precursor column was observed after formation, in a similar fashion to Ni arrays, indicating a significant portion of the drive current on axis during the experiment [32], in contrast to the 16 wire results discussed in this work. When MAGPIE is operated with a pre-pulse, comprising a linear ramp over 500 ns to 35 kA, current driven instabilities in the precursor column are also observed [33], and the variation in current in the precursor column for nested [34] and mixed wire [35] arrays is the subject of future investigations. It should be noted that much work is currently being carried out to determine the current distribution in the various array configurations, notably on the Zebra generator at the University of Nevada, Reno [36] and on the Angara 5-1 facility at Troitsk, Moscow [37].

In summary, for 16 and 32 wire Al and W arrays the current fraction in the precursor during experiment is low

($<3\%$), and this fraction appears to be slightly higher for tungsten than aluminum. It is clear, however, that further work must be carried out to determine the experimental array parameters that control the transfer of current to the array axis.

IV. COMPARISON TO COMPUTATIONAL MODELS

Both hydrodynamic (HD) and kinetic models were applied in order to further elucidate the formation mechanism of the precursor column. The hydrodynamic model is a simplified version of the three-dimensional (3D) Eulerian resistive magnetohydrodynamic "Gorgon" code developed by Chittenden *et al.* A full description can be found in Ref. [15]. The code performs explicit hydrodynamics on a Cartesian (x,y,z) Eulerian grid, using second order Van-Leer advection. The thermal and magnetic field diffusion equations are solved implicitly by iterative solution of matrix equations. The model is two temperature (electrons and ions) with local thermal equilibrium (LTE) ionization and a simple recombination radiation loss model. The radiation loss model is modified to include a probability of escape that allows a smooth transition to blackbody emission in the dense plasma regions. A cut-off density of 10^{-4} kg m^{-3} is used in order to represent the vacuum surrounding the pinch.

For the current study, this code is used in 1D cylindrical coordinates and magnetic field effects are neglected, and the model is therefore purely hydrodynamic (HD). A continuous flow of plasma is introduced at the boundary with a flow velocity and density consistent with the rocket model. An artificial "filtered" radiation output can be generated by summing radiation from regions of plasma with a temperature >45 eV, and this allows some comparison to experimental x-ray signals. The temperature chosen here is rather arbitrary in an attempt to more clearly discern the mechanisms at work, but is not in significant disagreement with the experimental measurements made at photon energies of 200–280 eV presented in Sec. III B. Cases for over-massed aluminum and tungsten were investigated.

The electron and ion temperatures and mass density for aluminum at selected times are given in Fig. 16. A 2 mm radius from the array axis is shown in each case, and the filtered radiation output for this run is given in the same figure (note that in this configuration the array does not implode). At 130 ns, the plasma shows a relatively broad low density profile as a standing shock develops. The electron and ion temperatures towards the axis (axis at 0 mm) have equilibrated, but the thermalization of streams at the shock give a high ion temperature here. The electron temperature towards the axis $\sim$70 eV and the radiation output is increasing, as density slowly rises, towards the first peak in the filtered x-ray signal.

At 155 ns, the first x-ray peak has been passed, and the electron and ion temperatures at the axis have dropped to $\sim$20 eV as a result of radiative loss. This cooling reduces the plasma temperature to below the energy cutoff for the radiation output, and so causes this signal to drop. The density profile is then compressed by the incoming plasma streams and begins to reduce in radius. The plasma on axis continues to be compressed to higher density, and the precursor column is present at 185 ns. As the column formation completes, the incoming plasma streams compress it on the axis, resulting in a small rise in the electron temperature, and this generates the second x-ray pulse. At 250 ns the column is observed as a stable shock, giving a high density object on the array axis. The electron temperature on axis is low, $\sim$15 eV, and the continued thermalization of plasma at the column edge gives a temperature of $\sim$30 eV here. This is below the "filter" for the radiation output, and so this remains at zero. Note that this radiation profile will be "hollow," i.e., low temperature at the column center with higher temperature surrounding region, in qualitative agreement with experimental observations.

The filtered x-ray output describes a two stage process for aluminum. The first peak is a result of increasing radiation loss due to a slow density rise. It is only following this peak that the broad initial density profile contracts to form the precursor column. The second peak is a result of compression of the column immediately after its formation by the incoming plasma streams. The timing of the first x-ray peak, at 142 ns, is similar to the experimental value of 155 ns, but the separation of the peaks is far greater in the simulation than observed in the experiment. It should be noted that the exact timing of the simulated x-ray peaks are heavily dependent of the radiation loss rate used in the model.

For a tungsten array simulation, the filtered x-ray output signal is significantly different (Fig. 17). The two stage signal from aluminum is not seen, and instead a single peak at 128 ns is generated. However, analysis of the density and temperature profiles shows that the processes which determine the x-ray pulse for aluminum are indeed occurring in a similar fashion for tungsten. The greater radiation loss rate for the heavier material causes these two processes to be almost simultaneous, and only a single peak is produced which comprises contributions from both. The timing of this signal is $\sim$50 ns earlier than is observed experimentally, which is a direct result of the inability of a fluid code to model the collisionless flow conditions in tungsten at early times. Note that the timing for aluminum of this first peak is much closer to the experiment. The aluminum plasma streams are collisional from early times, and so the fluid approximation is more appropriate and a reasonable agreement results. To investigate the effect of collisionality computationally, the application of a particle code is discussed next.

The kinetic approach uses a hybrid model comprising a particle description for ions and an electron fluid, and a full description can be found in [16]. Ions are injected at the array radius with a number density consistent from the rocket mass ablation model, and the experimental velocity of 1.5×10^5 ms^{-1}, which is assumed to be constant. Again, over-massed array configurations are used. Ions are advanced in configuration and velocity space in the usual particle-in-cell manner, and using a Monte Carlo collision algorithm. Interaction with the electron fluid is via a frictional force, which incorporates the temperature inequality and the electron-ion energy transfer time, representing the multiple scattering of ions from a Maxwellian distribution of field electrons. The radiation model used for the fluid code is utilized again here

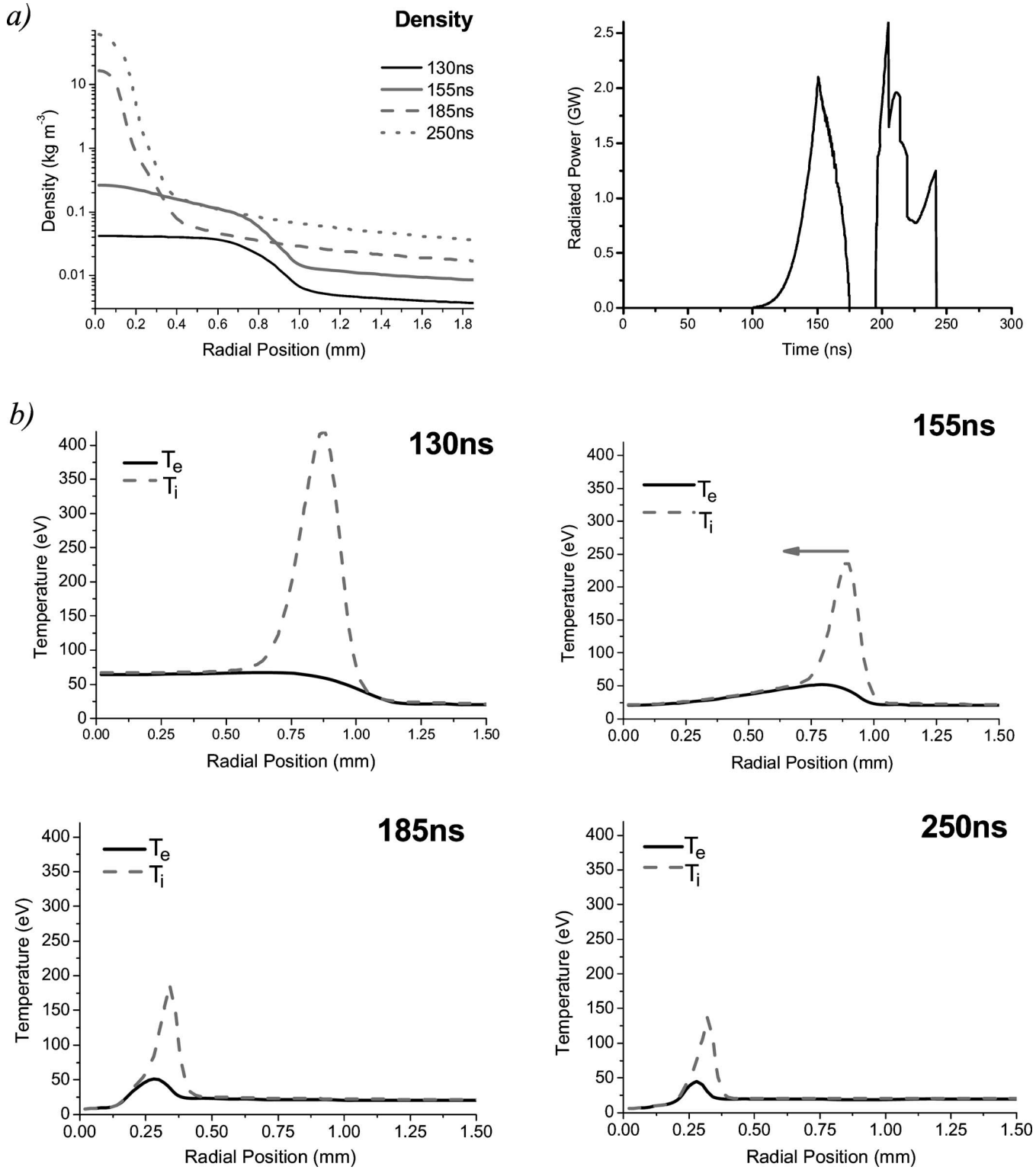

FIG. 16. Plots from hydrodynamic model results showing (a) Mass density profiles for selected times, along with filtered x-ray output, and (b) Electron and ion temperature profiles at selected times for simulated aluminum array. (Array axis is at 0 mm and the only first 2 mm radially from axis are simulated.).

to determine cooling rates for aluminum. Due to the lack of a simple reliable radiation loss model for tungsten, the same model is used to calculate cooling rates in tungsten.

Figure 5 of Ref. [16] shows the evolution of density profiles for aluminum and tungsten arrays. Aluminum shows a relatively well defined shock profile even at early times, resulting from the stagnation of the ions streams as they reach the array axis. Tungsten, however, shows a very broad flat profile for a long time. This is a result of the collisionless flow conditions of the ions streams at early times, and den-

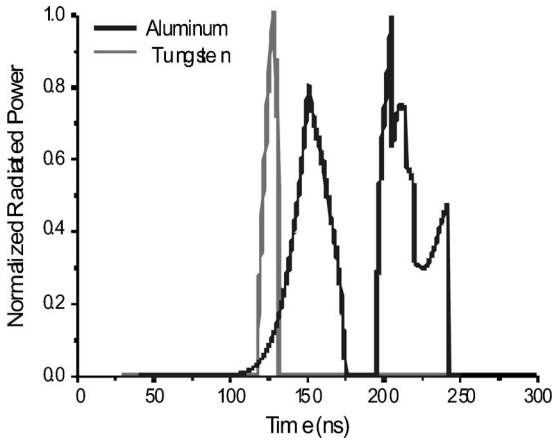

FIG. 17. Filtered x-ray output from hydrodynamic model for aluminum (black) and tungsten (dashed grey).

sity is peaked on axis due to the convergent flow configuration, rather than stagnation of the plasma streams.

The collapse of this initial profile occurs earlier in aluminum, and the column is fully formed by 160 ns at a diameter of ~1 mm. This does not occur in tungsten until 175 ns, and the formed column diameter is ~0.5 mm. The maximum density in both cases remains similar after formation, and both columns grow in radius as a result of the accruement of mass from the plasma streams. The on-axis ion temperature is seen to reduce as column formation occurs for both materials. At late times, the ion temperature in low at the column center, and a peak in the ion temperature at the edge of the column is observed where ions continue to thermalize, in a similar fashion to the fluid code results.

Both models show formation of a high density column forming on axis from a broad initial density profile for both aluminum and tungsten. In addition, after formation both descriptions show a peak in ion temperature at the edge of the shock which defines the formed column, while the column center has equilibrated to the electron temperature. This suggests a hollow emission profile as observed in the experiment. The macroscopic dynamics of precursor column formation appear to be well described in both cases.

The formation times, however, differ between the approaches. Aluminum column formation times agree reasonably well, but the HD code predicts tungsten column formation significantly earlier than observed either experimentally or in the kinetic model. The kinetic description shows a much broader initial density profile for W than Al, in line with the experimental observations. The fluid model shows the opposite case, the limiting factor being the onset of radiative loss, which is more delayed for Al than W, allowing the standing shock to grow to larger radii. These differences are a result of collisionless flow in tungsten plasma streams at early times, which fluid modeling is unable to account for. This occurs for some 40 ns after tungsten plasma streams reach the array axis, delaying the formation of the precursor column and the peak in the x-ray signal. If this approximate delay is simply added to the formation times and x-ray signal for the HD model results, a far better agreement with experiment is achieved. There is currently no x-ray signal comparison from the kinetic code, but column formation times for Al and W agree very well with the experimental values of 150–160 ns and 170–180 ns respectively.

The formation mechanism, described in detail above for the HD model, shows an inherently two stage process, the timings of which are determined by the array material. Collapse of the initial broad density profile occurs only after the first peak of the x-ray signal, as is observed experimentally. The second stage is a compression of the formed column, resulting in a small temperature rise. The delay between the two events is significantly smaller for tungsten than for aluminum, again in qualitative agreement with experiment. Materials of different atomic masses would be expected to fall between these two extremes, and show an x-ray signature with two peaks separated by a distance related to the radiation loss rate of the material. Preliminary investigations using the HD model show this is indeed the case. Nickel, for example, gives two filtered x-ray peaks separated by less than is seen for aluminum but greater than for tungsten. The absolute timing differences, however, are heavily dependent on the details of the radiation loss routines applied in the codes. These are notoriously difficult areas to clearly define, and further work on both experiment and computational radiation loss models is required.

The fluid approach is reasonable for the aluminum arrays investigated in this work, but the collisionality of tungsten plasma streams are fundamental to an accurate description. A kinetic description is required in the early stages of plasma stream interaction. At higher velocities, this may also become important in aluminum and even lower atomic number materials, and so is an essential part of the process. It may be possible to include the effects of early time collisionless flow in the fluid model by means of a collision operator, as described in Refs. [38,39], although this is essentially an approximation to the full kinetic approach. At later times, following the onset of collisionality, both the fluid and kinetic descriptions show a similar formation mechanism, and this correlates well to the experimental results.

On generators such as the *Z* machine, the distinction between materials is likely to be less significant. The higher current level and faster rise rate leads to the ablation of a considerably greater mass of material from the wires than on MAGPIE. The plasma flow is therefore likely to be collisional from early time, and for 20 mm arrays the interaction at the array axis will be dominated by collisional flow. The importance of collisionless plasma flow may increase significantly if the plasma flow velocity is high. For lower mass 20 mm diameter tungsten arrays this may indeed be the case [40], and for 40 mm diameter arrays, the inferred velocity of material streaming to the array axis may be as high as 4×10^5 ms^{-1} [41]. Plasma may counterstream at the array axis for a period of time, and therefore this behavior must be included in the modeling of these arrays.

V. TWISTED WIRE ARRAYS

In this modification, a 2.3 cm long, 16 mm diameter wire array was twisted at an angle of $\pi/4$, $\pi/2$, or $3\pi/4$ by rotation of the top electrode relative to the bottom electrode.

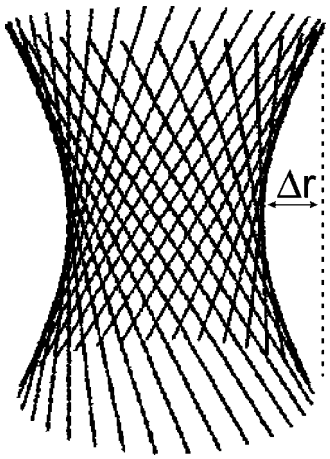

FIG. 18. Diagram of a 32 wire array with a $\pi/2$ twist, showing the reduction in radius along the z axis as a result of the twist.

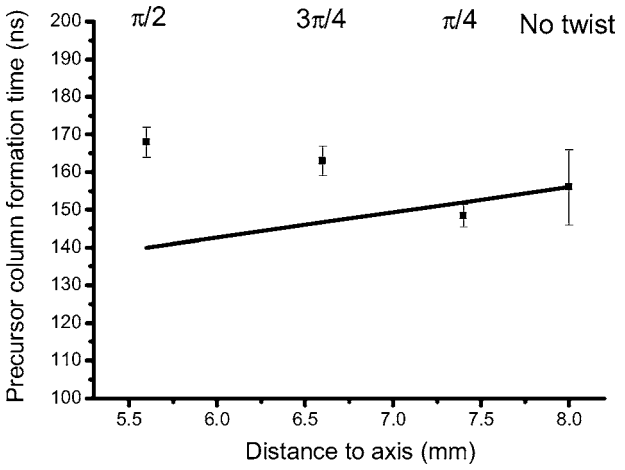

FIG. 19. Variation of precursor formation time at the array half height with distance of wires from array axis. Data (■) is shown with error bars, and solid line represents predicted formation time from time-of-flight variation at fixed velocity.

Twisted wire arrays were considered as a method of mitigating Rayleigh-Taylor (RT) instabilities during the implosion phase of an array, as was observed for uniform density gas-puff experiments with an "hourglass" axial distribution [42]. In this work twisted arrays are used to investigate properties of the precursor flow inside the array.

The smallest angle of rotation can be used to measure the azimuthally averaged radial distribution of the coronal plasma inside the array. The twisting effectively removes the azimuthal structures, formed by the collision of the streams from different wires, from the end-on images (shocks shown in Fig. 3). For twisted arrays the shocks are not seen due to averaging of the gradients along the probing path of the laser beam. This is shown for a 32 wire aluminum array in Fig. 10 of Ref. [22].

For arrays with larger angles of twist, the axial magnetic field B_z, generated inside the array is large enough to noticeably affect the dynamics of the inward flow of the coronal plasma. The precursor plasma column on the array axis is still formed, but this happens later and the delay increases with the twist angle. As this is increased, the distance Δr increases, and hence the distance from the wires to the array axis at the mid-plane of the array decreases (Fig. 18). The time of flight for plasma ablated from the wires reduces accordingly and it is expected that the precursor column should form at progressively earlier times as the twist angle is increased. Figure 19 shows the time of the precursor formation measured by radial streak photography in the middle of the array for the different twist angles. The solid line represents the predicted formation time from the reducing time of flight to the array axis, assuming fixed velocity, and is normalized to the experimental point for zero twist. The formation time for $\pi/4$ is earlier than for an untwisted array, and very similar to the flight time prediction. This suggests that small twist angles do not significantly disturb the plasma flow behavior inside the array. At larger twist angles, however, the precursor column formation time increasingly deviates from the time-of-flight predictions. Both $3\pi/4$ and $\pi/2$ twist angles display a later column formation time than untwisted arrays, despite wires being substantially closer to the array axis at the array midplane. This observed delay of the precursor formation could occur due to deceleration of the coronal plasma by the pressure of the axial magnetic field (B_z) generated inside the array, although precise mechanisms are unclear at present.

For arrays with a $\pi/2$ twist, the axial magnetic field generated in twisted wire arrays was measured using two magnetic probes (with opposite orientation of the turns), installed inside the array at the axial position at the end of the array, inside the hollow top electrode [43]. The measured value of B_z at ~150 ns was ~1.5 T, which corresponds to a magnetic field of ~3 T in the middle of the array. It should be emphasized that this estimate of the magnetic field in the middle of the array was obtained neglecting an effect of shielding of the magnetic field at the position of the probe by the electrode, and thus represents a lower estimate of the field inside the array.

Calculated (magnetostatic) values of B_z for the twist angle of $\pi/2$ suggest $B_z \sim 5$ T at time ~150 ns (assuming that the current is flowing through or very close to the wires and neglecting attenuation of the field by the currents induced in the electrodes). The fact that experimental and calculated values are reasonably close may indicate that the calculation assumptions are correct, in that the current flows close to the wires. It is important to note that if current carrying plasma from adjacent wires merged, current would be able to flow directly axially and no B_z would be measured in the experiment. If plasma streams remain discrete for a significant proportion of the array radius, a considerable amount of the drive current may be carried towards the array axis, and a B_z field would still be measured. However, in untwisted aluminum cylindrical arrays, streams are observed to interact (shock structures on Fig. 3) approximately 1 mm from the wire position. The persistence of the axial magnetic field therefore suggests that current primarily flows in regions no closer to the axis than 1 mm inside the array radius.

VI. SCALING AND APPLICATIONS OF THE PRECURSOR COLUMN

The precursor column demonstrates several interesting plasma physics processes occurring during its formation, in-

cluding transition from collisionless to collisional flow regimes, and the effect of radiation loss on the dynamics of the plasma. On the MAPGIE generator, precursor column densities shortly after formation are of the order of $10^{19}-10^{20}$ ions/cm^{-3} and temperatures of 80–100 eV are inferred, which vary with array material. These values lie in warm dense matter (WDM) regime. For the relatively long time scales on which the precursor column has been observed in this work (>200 ns) the constant or increasing density and decreasing temperature ensure the precursor column remains close to this region. By studying the behavior of the precursor column at different times during its lifetime, several different regions of parameter space may be accessible.

To investigate how the precursor column characteristics scale with generator, we can attempt to extend previous analyses to the *Z* Machine at Sandia National Laboratories (20 MA, 100 ns rise time) to see how this compares with published experimental data. Cuneo *et al.* [11] report that precursor structures with a FWHM diameter of 1.5–3 mm have been observed on axis at times $>0.5\ \tau_{stag}$ (where τ_{stag} is the stagnation time of the array on to the axis). Observations have not been made at times earlier than this at present. The precursor remains at constant radius for ~20 ns and then expands as the main array implosion begins at $\sim 0.75\ \tau_{stag}$, as discussed in Sec. III B. Analysis of time resolved x-ray pinhole cameras (XRPHC) indicates precursor radiation brightness temperatures of 25–30 eV at early time which rises to ~75 eV at the time that the main array mass implodes onto it. The following discussion continues the pressure balance approach, which describes the precursor column on MAGPIE well, for 20 mm diameter tungsten arrays on *Z*.

Section III C derived a relationship for the "equilibrium" radius of the precursor column immediately after formation as a function of the generator current, the ablation velocity and the temperature [see Eq. (4)]. This can be rearranged to give the temperature as a function of the radius at a given point in the current drive

$$(z+1)T(t) = \left[\frac{I^2[t - R_0/V_a]}{\int_0^{t-R_0/V_a} I^2(t)dt}\right]\frac{V_a m_{ion} R_{eq}}{2}. \qquad (10)$$

To determine the product $(z+1)T$ at a given point in the current drive, the equilibrium precursor radius, R_{eq}, and the ablation velocity, V_a, must be supplied. If the range of 1.5 to 3 mm given above is taken, the temperature product can be calculated for a range of ablation velocities as a function of time.

At very early times this value will clearly be unphysical, since the precursor column will not have formed. The onset of the formation process results from increasing radiation loss due to increasing on-axis density, which becomes comparable and then exceeds the kinetic energy flux from incoming plasma streams allowing collapse of the density profile. As the radiation loss rate is proportional to n_i^2, it is therefore the on-axis ion density which is central to the timing of the precursor column formation. The ion line density at the array axis as a function of time and current is given by the mass arriving at the axis derived from the rocket ablation model divided by the ion mass

$$n_{ion(axis)}(t) = \frac{\mu_0}{4\pi V_a R_0 m_{ion}} \int_0^{t-R_0/V_a} I^2(t)dt. \qquad (11)$$

In Al arrays on MAGPIE, ablated plasma streams are collisional from early times as they reach the axis, as is expected to be the case for 20 mm W arrays on *Z*. A delay in column formation occurs for W arrays on MAGPIE due to the lower ion number density ablated ($\propto 1/m_{ion}$) and a period of collisionless flow at the axis. To give an indication of when formation of the precursor column is likely to occur on *Z*, we will therefore examine the ion density in aluminum on MAGPIE at the time of formation observed in experiments. The first peak in the soft x-ray signature for Al occurs at an average time of 155 ns after current start (see Fig. 5), and this indicates when radiation-driven collapse and column formation has begun. The ion line density at the array axis at this time is $\sim 6\times 10^{18}$ m^{-1}. If the column formation processes described in this work on MAGPIE occur in a similar fashion on *Z*, this represents a "critical" ion density, $n_{i,crit}$, at which point the formation processes are occurring and the precursor column will form. The time at which $n_{i,crit}$ is reached at the axis during an experiment therefore represents the earliest time at which the precursor column is expected to form.

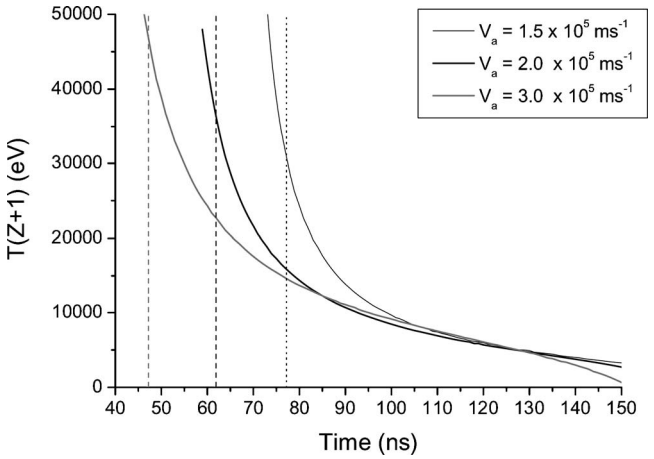

FIG. 20. Calculated variation of the product $T(Z+1)$ with time for a precursor column of fixed diameter (1.5 mm) for three ablation velocities. Dashed vertical lines indicate expected precursor column formation time (see text).

The product $(z+1)T$ for a fixed column diameter of 1.5 mm calculated from Eq. (11) is presented in Fig. 20 for a range of ablation velocities. These calculations assume the array configuration is again over-massed and that the main implosion phase does not occur. The dashed vertical line is the time at which the ion line density at the axis first exceeds the critical value of 6×10^{18} m^{-1}. Values to the left of this line (i.e., earlier in time) are prior to column formation and therefore unphysical. The value of $(Z+1)T$ at $n_{i,crit}$ is greatest for the largest ablation velocity, and this decreases with decreasing velocity. Rapid cooling is apparent for all ablation

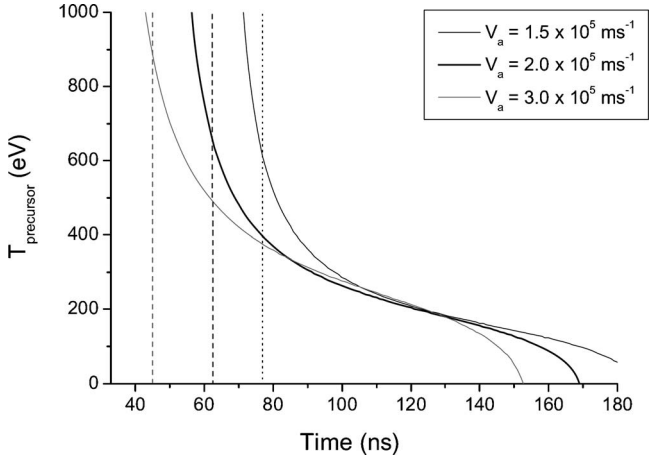

FIG. 21. Calculated variation temperature with time for a precursor column of fixed diameter (1.5 mm) for three ablation velocities, using a CE ionization model. Dashed vertical lines indicate expected precursor column formation time (see text).

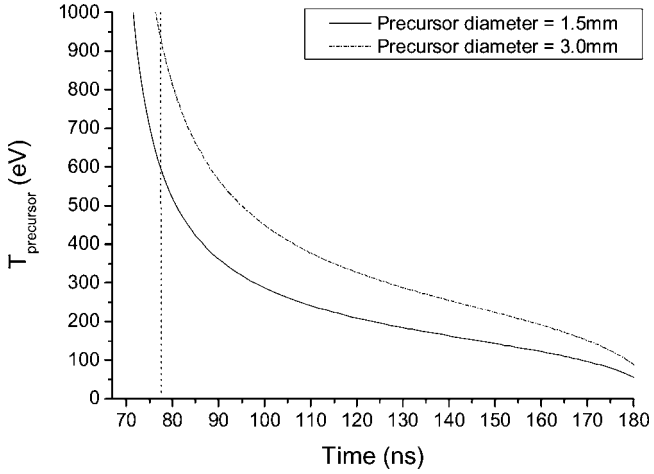

FIG. 22. Calculated variation temperature with time for precursor column of 1.5 mm and 3 mm diameter using fixed ablation velocity. Dashed vertical line indicates expected precursor column formation time (see text)

velocities and the plots converge to similar values after ~100 ns.

The time at which the precursor column is expected to form varies considerably with ablation velocity. The formation time for the lowest velocity (1.5×10^5 ms^{-1} gives 77 ns) is 30 ns later than for the highest velocity (3×10^5 ms^{-1} gives 47 ns). This difference represents a third of the current rise time on *Z* and is therefore highly significant in the understanding of pre-implosion processes in these arrays. It should be noted that the line of $n_{i,crit}$ assumes collisional flow dominates interaction at the axis, and this would move later in time for a given ablation velocity if collisionless flow is important. It should also be noted that the $n_{i,crit}$ line position in time is relatively insensitive to changes in the current shape for *Z*. The fast high current rise dominates the process, and changes in the peak current reached (18–20 MA) and the inclusion of the experimental 1 MA "foot pulse" changes this position by <2 ns. In addition to these features there is also a prepulse current which rises to ~45 kA over 300 ns. If the ablation velocity and plasma streaming behavior are similar during this period it is unlikely that the mass ablated during the prepulse will affect the time of formation of the precursor column, however experiments to investigate this early time behavior are required to clarify this.

To estimate a temperature for the precursor column the coronal equilibrium model used in the MAGPIE calculations is again used here, and the resulting plots are given in Fig. 21. The temperature of the precursor column at $n_{i,axis} > n_{i,crit}$ varies significantly with the ablation velocity assumed. For the lowest velocity the temperature is ~600 eV at formation (77 ns) and drops to ~200 eV by 130 ns. Increasing this velocity by a factor of 2 gives a precursor column which forms at 47 ns with a temperature of ~900 eV and which again drops to ~200 eV by 130 ns. The calculated temperatures shortly after formation do not contradict experimental observations on *Z* (see Figs. 4 and 7 in [11]).

The above estimates are obtained using a precursor column diameter which is constant in time to allow a solution in the equilibrium situation. The real variations in the precursor column temperature after formation may be different due to changes in the precursor diameter with time during the experiment, and this should be investigated to further this interpretation. To provide some indication of the variation of the calculated temperature with column diameter, Eq. (11) can be evaluated for 1.5 mm and 3 mm diameter columns using a fixed ablation velocity of 1.5×10^5 ms^{-1} and again using a CE ionization model to recover a temperature. These plots are given in Fig. 22. The change in precursor diameter does not affect the time at which $n_{i,crit}$ is reached during the current drive, but the larger precursor is formed with a higher temperature. The pressure balance model used here dictates that the larger precursor is required to maintain a higher temperature in order to balance plasma stream kinetic energy. At formation the 3 mm diameter precursor is ~950 eV, while the 1.5 mm diameter column is ~600 eV, and even at late times the difference in temperature is >50 eV.

It is interesting to compare the time at which the "critical" ion density at axis is reached for these estimations with the experimental times at which precursor structures have been observed for 20 mm diameter tungsten arrays on *Z*. The average stagnation time for these arrays is 95.5 ns, and so the timing of the earliest observation of the precursor structures at the array axis corresponds to ~48 ns on the plots in Figs. 20–22 in this paper. The time at which $n_{i,crit}$ is reached, and hence the time at which the precursor column should form and be observed (dashed lines on plots), is calculated to be later than the experimental results above for both of the two lower velocities investigated. Only the highest velocity of $V_a=3\times10^5$ ms^{-1} yields a timing comparable to observations. For comparison, one can also consider the time of flight (TOF) of ablated plasma from the array radius to the axis for each of the ablation velocities investigated here. For the lowest velocity this TOF is 67 ns, and no ablated material will have reached the axis by the time of the experimental observation of a precursor structure at 48 ns ($0.5\tau_{stag}$). Similarly for $V_a=2\times10^5$ ms^{-1} the TOF is 50 ns, and plasma has barely reached the axis by the time precursor structures are

observed. The velocity of material streaming towards the array axis must therefore be greater than 2×10^5 ms^{-1} even if the precursor column forms immediately as streams collide at the axis. For the highest velocity, however, the TOF is 33 ns which allows a brief period of increasing on-axis density before $n_{i,\mathrm{crit}}$ is reached, and the precursor column is expected to form at ~47 ns ($\sim0.5\tau_{stag}$).

This high ablation velocity fits well with the formation time of the precursor column from experiments, but is significantly higher than has been calculated in [11] (1.4 ± 0.3 ms^{-1}) and references therein. This would give an anomalously low mass ablation rate at the wires which is inconsistent with the fitting of implosion trajectories carried out in [11]. One explanation for this discrepancy could be suggested by comparison to experimental observations of the ablation dynamics of wire arrays. It has been reported by many authors (e.g., [21,44,45] and references therein) that the plasma ablated from wires and ejected towards the array axis is periodically modulated in the axial direction—the "ablation wavelength." For tungsten, this wavelength is 250 μm. In addition, experiments demonstrate that gaps in the wire cores are subsequently formed indicating that mass ablation is not uniform axially, and mass ablation is greater at some points than at others. Some points along the wire length may eject material with a high velocity, which would then satisfy the early formation time of the precursor column, but there must then also be regions where mass ablation is high to facilitate wire breakage and the start of the implosion.

From the rocket model, the mass ablated at time t can be written as

$$\delta m = \frac{1}{V_a}\left[\left(\frac{\mu_0}{4\pi R_0}\right)\int_0^t I^2 dt\right]. \tag{12}$$

For each wire in an array, the values in square brackets in Eq. (13) are the same for all points along the wire in the axial direction, and the mass ablation rate therefore scales as $1/V_a$. As the simplest approximation, we can consider that the velocity of the plasma flow is two component: some fraction of the wire length f is ablated with a high velocity V_1, and the remainder of the wire length is then ablated with a lower velocity V_2. In order to be consistent with the trajectory fits presented in [11] the average mass ablation rates resulting from these two velocities must be equal to the overall ablation rate reported by the average ablation velocity $\langle V\rangle$. Given the $1/V$ scaling above this can be written as

$$\frac{f}{V_1} + \frac{(1-f)}{V_2} = \frac{1}{\langle V\rangle}. \tag{13}$$

As an example, we can apply this two-component model to the 20 mm arrays on *Z*. The fraction ablating can be taken as 0.5 since the axial modulation of ablated plasma streams is observed to be periodic. If the mass ablated from the high velocity regions becomes evenly distributed in the axial direction as it reaches the axis, the time at which the precursor will form is then $n_{i,crit}/f=2n_{i,crit}$. The rapidly rising current pulse means that this value is reached shortly after $n_{i,crit}$ itself and an ablation velocity of 3.5×10^5 ms^{-1} allows the precursor to form at 0.5 τ_{stag}. This velocity is the minimum required to match the experimental observations of precursor formation. The average ablation velocity $\langle V\rangle$ can be taken from [11] to be 1.4×10^5 ms^{-1}. For this situation, the lower ablation velocity V_2 can be determined by rearranging Eq. (14) and setting $f=0.5$

$$V_2 = \frac{\langle V\rangle V_1}{2V_1 - \langle V\rangle}. \tag{14}$$

For the values discussed above $V_2=0.9\times10^5$ ms^{-1}. From Eq. (13), this velocity component accounts for 85% of the mass ablated up to the start of the implosion of the array ($\sim0.6\tau_{stag}$). The use of a two-component flow velocity can be used to explain both the relatively early time formation of the precursor column and the observed implosion trajectory. It would be useful to examine 20 mm arrays earlier in time than 0.5 τ_{stag} in order to place an upper limit on V_1, and the expected high collisionality of the ablated plasma streams is likely to give a good indication of the experimental time of flight from emission based diagnostics. As this velocity tends to very large values, the velocity V_2 tends to $\langle V\rangle/2$ and the wires will burn through completely at the positions with a high mass ablation rate. To further investigate these ideas, comparisons to data from different generators and with different array diameters must be carried out, and this will be the subject of future studies.

The high contrast in density between the precursor column and the plasma flow may allow studies of radiating shocks, and in particular cooling lengths across the shock, which was clearly measurable in the experimental results given in this study. Such a stable area radiator may have applications in opacity measurements as an alternative to the secondary hohlraum method used in [46], as large area soft XUV backlighter, or as part of a Ti collisional laser as suggested by several authors including in [47]. The absorption spectroscopy of well-characterized warm dense matter targets is also of considerable interest, and the use of different material columns to provide different characteristics (diameter, temperature, electron/ion density) gives good flexibility for this system. The precursor column remains stable for >200 ns in the work presented here, and properties such as the variation in absorption spectrum as the column cools can therefore be measured in a single experiment.

The lifetime of the precursor column depends directly on the drive current rise time. For some applications it may be possible to utilize long rise time machines, to produce an even longer-lived source. When used in conical geometry, the continuous injection of mass towards the array axis forms a conical shock and drives a plasma jet significant distances beyond the array height [48]. These well collimated, high Mach number experimental jets are hydrodynamically scalable to astrophysical objects such as young stellar object (YSO) jets. Experiments on MAGPIE studying their behavior in different ambient conditions [49,50] have effectively demonstrated the flexibility and astrophysical relevance of these experiments [51,52]. Using a long rise time generator (e.g., Atlas [53] 30 MA, 4 μs rise time) very high aspect ratio jets could be produced to study the effect of multiple jet

target interactions on dynamical properties including jet collimation and internal shock formation. A further interesting possibility is the use of spherical geometry as has been investigated on MAGPIE [54,55] and computationally for conditions on the Z generator [56]. Spherical precursor plasma flow produces a central object, analogous to the cylindrical array precursor column, of significantly higher density than in cylindrical geometry.

VII. CONCLUSIONS

The phenomenon of the compact precursor column in wire array z pinches occurs due to an intrinsic feature of the plasma formation process from the initially solid wires. At the very beginning of the current pulse the wires are rapidly converted into a heterogeneous structure with dense cold cores surrounded by a low-density hot coronal plasma. This coronal plasma is continuously formed from the wire cores and injected by the $\mathbf{J}\times\mathbf{B}$ force towards the axis of a wire array. Stagnation of this plasma flow at the array axis creates a dense and stable precursor plasma column.

The precursor column formation process shows three distinct stages: (i) Broad initial density profile, (ii) rapid contraction to small diameter, (iii) slow expansion following formation. The timing of these stages and the form of the associated x-ray signal are a direct result of the collisionality of the ablated streaming plasma. For wire arrays from different materials the velocity of the coronal plasma flowing to the array axis appears approximately the same from experiment. The corresponding kinetic energy of the ions, however, is significantly higher for materials with higher atomic numbers, and the interaction of the plasma streams near the array axis remains collisionless for a longer time. This leads to a delay between the first arrival of the plasma to the axis and the formation of a dense precursor column, as well as a variation in the diameter of the on-axis plasma at early times: collisionless W streams give a broader initial profile than collisional Al streams.

The rapid contraction of the broad initial density profile occurs when the total energy radiated from the plasma approximately equals the kinetic energy accumulated at the axis. Correlation of soft x-ray emission to gated x-ray camera images confirms that the small diameter fully formed column appears only after the peak of the formation x-ray signal. The resulting rapid contraction occurs over $\sim$10 ns for both Al and W, and the fully formed precursor column results.

After formation, the dense precursor plasma column remains remarkably stable until the final stagnation of the array for imploding loads, and does not show development of $m=0,1$ MHD instabilities for a significant period of time for overmassed loads. Typical time scales are $\sim$100 ns for W and $\sim$300 ns for Al. This absence of MHD instabilities provides an upper estimate of the fraction of the total current which might flow in this plasma column as being $<1\%$ and $<2\%$ for Al and W, respectively. A larger degree of instability, inferring larger proportions of the drive current in the precursor, is observed for some materials (in particular Ni) and for low wire number arrays. The magnitude of current in Al and W precursor columns is not sufficient for the magnetic confinement of the precursor plasma column, the confinement is instead provided by the kinetic pressure (ρV^2) of the radially converging flow of the coronal plasma. A simple model for scaling of the equilibrium precursor radius immediately after formation with atomic number developed from pressure balance considerations shows good agreement with the experimental data for wire arrays formed from nine materials (C, Al, Ti, Fe, Ni, Cu, Mo, W, and Au).

The continuous accumulation of material in the precursor implies that ablation of the wire cores continues throughout the current drive time which indicates that a significant portion of the current remains in close proximity to the wire cores. This conclusion is supported by the experiments with twisted wire arrays, in which generation of an axial magnetic field inside the array was detected. This magnetic field could only persist if the current follows close to the wire cores and is not convected towards the axis by the coronal plasma stream, which merge at large radii. When the measured axial magnetic field is sufficiently high, the inward motion of the coronal plasma is affected resulting in a delay in the formation of the precursor plasma column. This delay increases with twist angle, indicating that the plasma flow to the axis is increasingly inhibited by the increasing axial magnetic field. The mechanism for this is unclear at present. The small increase in current in W array precursors over Al array precursors, and the large increase observed in Ni precursor columns, indicates that plasma flow conditions vary significantly with array material and that this requires further investigation.

The expansion rate of the precursor column after formation is greater for aluminum than for tungsten. Values are similar to those predicted by two simple models, one assuming constant density and another assuming constant temperature, but the increasing deviation from the constant temperature model suggests the column is cooling with time. Using the experimental expansion rates and a coronal equilibrium (CE) charge state model, the temperature variation with time for Al and W can be calculated. Initial temperatures are similar for local thermal equilibrium (LTE) ionization and slightly higher for coronal equilibrium (CE) ionization than the range inferred from previous XUV spectroscopy data. Following formation cooling rates are approximately 0.55 eV/ns (CE) and 0.34 eV/ns (LTE) for Al, and 0.65 eV/ns (CE) and 0.29 eV/ns (LTE) for tungsten.

Both kinetic and fluid computational models describe the formation of the precursor well, but collisionality at early times is essential in the description to reproduce the experimentally observed formation times. Modeling suggests that the formation mechanism is an inherently two-stage process. The first stage shows increasing radiation as on-axis density increases. The rapid collapse phase then occurs and the second part of the x-ray signal is a result of a compression of the formed column by the ablated plasma streams. The soft x-ray emission during precursor column formation comprises contributions from both these processes, and again it is array material which determines their relative timings. Aluminum arrays show discrete peaks for each stage, which are relatively widely separated in time, whereas tungsten shows only a single peak as the two processes are nearly co-incident. This mechanism is in good qualitative agreement with the experimentally recorded x-ray signals.

The aluminum and tungsten arrays studied in detail in this work represent two extremes with regard to the atomic number and mass of materials commonly used for wire array z pinches. Other intermediate materials would show different precursor column formation time, formation x-ray signatures, and expansion rate following formation. On MAGPIE, these materials would be expected to display behavior which is intermediate between aluminum and tungsten, due to the fact that the determinate processes are dependent on mass and atomic number. The formation time depends on the atomic mass to determine collisionality, and on atomic number which determines the rate of radiative energy loss. The atomic number dependence of the radiation loss rate also determines the separation of the formation x-ray peaks as elucidated from hydrodynamic modeling. The rate of expansion following column formation also varies inversely as the atomic mass. This expected variation was clearly observed in the trend of the minimum diameter of the precursor column observed for several different materials in this study. The precursor column behavior on other generators would be expected to vary in a similar fashion.

The rocket ablation model [21] generally gives a good description of the mass ablated from array wires cores during an experiment, and has been widely used in analytical estimations and computational modeling, including in this work. Predictions from this model do not always accurately describe the data, and a better agreement with precursor column data from the *Z* machine at Sandia National Laboratory is achieved using a 2 ablation velocity rocket model. This is a direct indication of the requirement to more fully understand the ablation behavior of wire array z pinches. Further investigations must be carried out to more clearly define the parameters of the plasma flow conditions, including how the plasma flow velocity, temperature and density varies with time, configuration, and array material. More importantly, the details of the ablation phase of wire arrays must be determined as it is from this that all subsequent processes are derived. It may then be feasible to accurately model the entire array experiment with sufficient accuracy to allow reliable extrapolation to future higher current generators.

ACKNOWLEDGMENTS

The authors gratefully acknowledge many interesting discussions on the physics of precursor plasma in wire array z pinches with Dr. Jack Davis, Dr. Sasha Velikovich, and Dr. Bob Terry of the Naval Research Laboratories, with Dr. Keith Matzen, Dr. Chris Deeney, Dr. Rick Spielman, Dr. Tom Sanford, Dr. Mike Cuneo, and Dr. Gordon Chandler of the Sandia National Laboratories and with Professor David Hammer of Cornell University. The authors also thank the Target Fabrication Group at AWE Plc. who kindly produced the tungsten step wedge used for the radiography analysis. This research was sponsored by the NNSA under DOE Cooperative Agreement DE-F03-02NA00057.

[1] I. K. Aivazov, V. D. Vikharev, G. S. Volkov, L. B. Nikandrov, V. P. Smirnov, and V. Ya. Tsarfin, Sov. J. Plasma Phys. **14**, 110 (1988).
[2] C. Deeney, P. D. LePell, B. H. Failor, S. L. Wong, J. P. Apruzese, K. G. Whitney, J. W. Thornhill, J. Davis, E. Yadlowsky, R. C. Hazelton, J. J. Moschella, T. Nash, and N. Loter, Phys. Rev. E **51**, 4823 (1995).
[3] E. J. Yadlowsky, J. J. Moschella, R. C. Hazelton, T. B. Settersten, G. G. Spanjers, C. Deeney, B. H. Failor, P. D. LePell, J. Davis, J. P. Apruzese, K. G. Whitney, and J. W. Thornhill, Phys. Plasmas **3**, 1745 (1996).
[4] S. V. Lebedev, I. H. Mitchell, R. Aliaga-Rossel, S. N. Bland, J. P. Chittenden, A. E. Dangor, and M. G. Haines, Phys. Rev. Lett. **81**, 4152 (1998).
[5] I. K. Aivazov, V. D. Vikharev, G. S. Volkov, L. B. Nikandrov, V. P. Smirnov, and V. Ya. Tsarfin, JETP Lett. **45**, 28 (1987).
[6] J. P. Chittenden, S. V. Lebedev, A. R. Bell, R. Aliaga-Rossel, S. N. Bland, and M. G. Haines, Phys. Rev. Lett. **83**, 100 (1999).
[7] R. F. Benjamin, J. S. Pearlman, E. Y. Chu, and J. C. Riordan, Appl. Phys. Lett. **39**, 848 (1981).
[8] W. F. Noh, J. Comput. Phys. **72**, 78 (1987).
[9] L. J. Suter, A. R. Thiessen, F. Ze, R. Kauffman, R. H. Price, V. C. Rupert, V. W. Slivinsky, and C. Wang, Rev. Sci. Instrum. **68**, 838 (1997).
[10] C. A. Coverdale, C. Deeney, M. R. Douglas, J. P. Apruzese, K. G. Whitney, J. W. Thornhill, and J. Davis, Phys. Rev. Lett. **88**, 065001 (2002).
[11] M. E. Cuneo, E. M. Waisman, S. V. Lebedev *et al.*, Phys. Rev. E **71**, 046406 (2005).
[12] T. J. Nash *et al.*, Phys. Plasmas **6**, 2023 (1999).
[13] R. E. Olson *et al.*, Fusion Technol. **35**, 260 (1999).
[14] S. C. Bott, J. B. A. Palmer, D. J. Ampleford, S. N. Bland, J. P. Chittenden, and S. V. Lebedev, Rev. Sci. Instrum. **75**, 3944 (2004).
[15] J. P. Chittenden, S. V. Lebedev, C. A. Jennings, S. N. Bland, and A. Ciardi, Plasma Phys. Controlled Fusion **46**, B457 (2004).
[16] M. Sherlock, J. P. Chittenden, S. V. Lebedev, and M. G. Haines, Phys. Plasmas **11**, 1609 (2004).
[17] I. H. Mitchell, J. M. Bayley, J. P. Chittenden, J. F. Worley, A. E. Dangor, and M. G. Haines, Rev. Sci. Instrum. **67**, 1533 (1996).
[18] S. N. Bland, D. J. Ampleford, S. C. Bott, S. V. Lebedev, J. B. A. Palmer, S. A. Pikuz, and T. A. Shelkovenko, Rev. Sci. Instrum. **75**, 3941 (2004).
[19] R. B. Spielman, L. E. Ruggles, R. E. Pepping, S. P. Breeze, J. S. McGum, and K. W. Struve, Rev. Sci. Instrum. **68**, 784 (1997).
[20] S. V. Lebedev, R. Aliaga-Rossel, S. N. Bland, J. P. Chittenden, A. E. Dangor, M. G. Haines, and I. H. Mitchell, Phys. Plasmas **6**, 2016 (1999).
[21] S. V. Lebedev, F. N. Beg, S. N. Bland, J. P. Chittenden, A. E. Dangor, M. G. Haines, K. H. Kwek, S. A. Pikuz, and T. A.

Shelkovenko, Phys. Plasmas **8**, 3734 (2001).
[22] S. V. Lebedev, F. N. Beg, S. N. Bland, J. P. Chittenden, A. E. Dangor, M. G. Haines, S. A. Pikuz, and T. A. Shelkovenko, Laser Part. Beams **19**, 355 (2001).
[23] S. V. Lebedev, J. P. Chittenden, D. J. Ampleford, F. N. Beg, S. N. Bland, C. Jennings, M. Sherlock, M. G. Haines, S. A. Pikuz, T. A. Shelkovenko, and D. A. Hammer, in *Conference Proceedings Beams/DZP*, June 2002, Albuquerque, NM, USA.
[24] S. N. Bland, S. V. Lebedev, D. J. Ampleford, S. C. Bott, J. P. Chittenden, J. B. A. Palmer, C. Jennings, and J. Rapley, in *6th International Conference on Dense Z-pinches*, 2005, Oxford, UK.
[25] G. N. Hall, S. A. Pikuz, T. A. Shelkovenko, S. N. Bland, S. V. Lebedev, D. J. Ampleford, J. B. A. Palmer, S. C. Bott, J. Rapley, J. P. Chittenden, and J. P. Apruzese, Phys. Plasmas **13**, 082701 (2006) .
[26] D. Salzman, *Atomic Physics in Hot Plasmas—CE ionisation* (Oxford University Press, Oxford, 1998), pp. 127–129.
[27] D. R. Farley, K. G. Estabrook, S. G. Glendinning, S. H. Glenzer, B. A. Remington, K. Shigemori, J. M. Stone, R. J. Wallace, G. B. Zimmerman, and J. A. Harte, Phys. Rev. Lett. **83**, 1982 (1999).
[28] S. V. Lebedev, F. N. Beg, S. N. Bland, J. P. Chittenden, A. E. Dangor, M. G. Haines, S. A. Pikuz, T. A. Shelkovenko, and D. A. Hammer, Rev. Sci. Instrum. **27**, 671 (2001).
[29] N. R. Pereira *et al.*, J. Appl. Phys. **55**, 704 (1984).
[30] S. V. Lebedev, D. J. Ampleford, S. N. Bland, S. C. Bott, J. P. Chittenden, J. Goyer, C. A. Jennings, M. G. Haines, G. N. Hall, D. A. Hammer, J. B. A. Palmer, S. A. Pikuz, T. A. Shelkovenko, and T. Christoudias, Plasma Phys. Controlled Fusion **47**, A91–A108 (2005).
[31] F. N. Beg, S. V. Lebedev, S. N. Bland, J. P. Chittenden, A. E. Dangor, and M. G. Haines, IEEE Trans. Plasma Sci. **30**, 552 (2002).
[32] S. N. Bland, S. V. Lebedev, F. N. Beg, H. Kwek, J. P. Chittenden, and M. G. Haines, in *5th International Conference on Dense Z-pinches*, 2002, Albuquerque, NM, USA.
[33] F. N. Beg, S. V. Lebedev, S. N. Bland, J. P. Chittenden, A. E. Dangor, and M. G. Haines, Phys. Plasmas **9**, 375 (2002).
[34] S. N. Bland, S. V. Lebedev, J. P. Chittenden, C. Jennings, and M. G. Haines, Phys. Plasmas **10**, 1100 (2003).
[35] S. N. Bland, S. V. Lebedev, D. J. Ampleford, S. C. Bott, and J. P. Chittenden, Phys. Plasmas **9**, 2293 (2002).
[36] V. V. Ivanov, G. S. Sarkisov, P. J. Laca *et al.*, IEEE Trans. Plasma Sci. (to be published).
[37] E. V. Grabovski, G. G. Zukakishvili, K. N. Mitrofanov, G. M. Oleinik, and P. V. S. I. N. Frolov, Plasma Phys. Rep. **32**, 32 (2006).
[38] R. L. Berger, J. R. Albritton, C. J. Randall, E. A. Williams, W. L. Kruer, A. B. Langdon, and C. J. Hanna, Phys. Fluids B **3**, 3 (1991).
[39] P. W. Rambo and J. Denavit, Phys. Plasmas **1**, 4050 (1994).
[40] D. B. Sinars, M. E. Cuneo, E. P. Yu, S. V. Lebedev, K. R. Cochrane, B. Jones, J. J. MacFarlane, T. A. Melhorn, J. L. Porter, and D. F. Wenger, Phys. Plasmas **13**, 056318 (2006).
[41] T. J. Nash, M. E. Cuneo, R. B. Spielman, G. A. Chandler, R. J. Leeper, J. F. Seaman *et al.*, Phys. Plasmas **11**, 5156 (2004).
[42] M. R. Douglas, C. Deeney, and N. F. Roderick, Phys. Rev. Lett. **78**, 4577 (1997).
[43] S. N. Bland *et al.*, in *1st International Workshop on the Physics of Wire Array Z-pinches*, March 1999, Pitlochry.
[44] B. Jones *et al.*, Phys. Rev. Lett. **95**, 225001 (2005).
[45] S. V. Lebedev, F. N. Beg, S. N. Bland, J. P. Chittenden, A. E. Dangor, M. G. Haines, S. A. Pikuz, and T. A. Shelkovenko, Phys. Rev. Lett. **85**, 98 (2000).
[46] P. T. Springer *et al.*, J. Quant. Spectrosc. Radiat. Transf. **58**, 927 (1997).
[47] J. P. Chittenden, S. V. Lebedev, S. N. Bland, J. Ruiz-Camacho, F. N. Beg, and M. G. Haines, Laser Part. Beams **19**, 323 (2001).
[48] S. V. Lebedev, J. P. Chittenden, F. N. Beg, S. N. Bland, A. Ciardi, D. Ampleford, M. G. H. S. Hughes, A. Frank, E. G. Blackman, and T. Gardiner, ApJ **564**, 113 (2002).
[49] D. J. Ampleford, S. V. Lebedev, A. Ciardi, J. P. Chittenden, S. N. Bland, S. C. Bott, J. Rapley, M. Sherlock, C. A. Jennings, A. Frank, and T. Gardiner, AIP Conf. Proc. **703**, 443 (2004).
[50] D. J. Ampleford, S. V. Lebedev, S. N. Bland, A. Ciardi, M. Sherlock, J. P. Chittenden, and M. G. Haines, AIP Conf. Proc. **651**, 321 (2002).
[51] S. V. Lebedev, D. J. Ampleford, A. Ciardi, S. N. Bland, J. P. Chittenden, M. G. Haines, A. Frank, E. G. Blackman, and A. Cunningham, ApJ **616**, 988 (2004).
[52] A. Ciardi, S. V. Lebedev, D. J. Ampleford, J. P. Chittenden, S. N. Bland, M. Sherlock, J. Rapley, S. C. Bott, and C. Jennings, AIP Conf. Proc. **703**, 447 (2004).
[53] H. A. Davis *et al.*, Jpn. J. Appl. Phys., Part 1 **40**, 930 (2001).
[54] S. V. Lebedev, D. J. Ampleford, S. N. Bland, S. C. Bott, and G. N. Hall, in *6th International Conference on Dense Z-Pinches*, 2005, Oxford, UK 25–28th July.
[55] C. A. Jennings, J. P. Chittenden, A. Ciardi, M. Sherlock, S. V. Lebedev, D. J. Ampleford, S. N. Bland, S. C. Bott, G. N. Hall, and J. Rapley, in *6th International Conference on Dense Z-Pinches*, 2005, Oxford, UK, 25–28th July.
[56] T. J. Nash, D. H. McDaniel, R. J. Leeper, C. D. Deeney, T. W. L. Sanford, K. Struve, and J. S. DeGroot, Phys. Plasmas **12**, 052705 (2005).